

**INVESTIGATION OF FLUX ENHANCEMENT OF MICROFILTRATION MEMBRANE  
BY USING COMPUTATIONAL FLUID DYNAMICS TECHNIQUE**

**KRITSANA SAIYOOD**

**A THESIS SUBMITTED IN PARTIAL FULFILLMENT  
OF THE REQUIREMENTS FOR THE DEGREE OF  
MASTER OF ENGINEERING IN CHEMICAL ENGINEERING  
FACULTY OF ENGINEERING  
KING MONGKUT'S INSTITUTE OF TECHNOLOGY LADKRABANG  
2014  
KMITL-2014-EN-M-230-199**

INVESTIGATION OF FLUX ENHANCEMENT OF MICROFILTRATION MEMBRANE  
BY USING COMPUTATIONAL FLUID DYNAMICS TECHNIQUE

KRITSANA    SAIYOOD

A THESIS SUBMITTED IN PARTIAL FULFILLMENT  
OF THE REQUIREMENTS FOR THE DEGREE OF  
MASTER OF ENGINEERING IN CHEMICAL ENGINEERING  
FACULTY OF ENGINEERING  
KING MONGKUT'S INSTITUTE OF TECHNOLOGY LADKRABANG  
2014  
KMITL-2014-EN-M-230-199

COPYRIGHT 2014

FACULTY OF ENGINEERING

KING MONGKUT'S INSTITUTE OF TECHNOLOGY LADKRABANG

หัวข้อวิทยานิพนธ์	การศึกษาการเพิ่มพลังค์ของไมโครฟิลเตรชันเมมเบรนด้วยเทคนิคพลศาสตร์ของไหลเชิงคำนวณ
นักศึกษา	นายกฤษณะ สายหยุด
รหัสประจำตัว	53611606
ปริญญา	วิศวกรรมศาสตรมหาบัณฑิต
สาขาวิชา	วิศวกรรมเคมี
พ.ศ.	2557
อาจารย์ที่ปรึกษาวิทยานิพนธ์	ดร.วัลย์รัตน์ จันทน์อัมพร
อาจารย์ที่ปรึกษาวิทยานิพนธ์ร่วม	ดร.สันติ วัฒนานุสรณ์

### บทคัดย่อ

ปัจจุบันนี้กระบวนการกรองด้วยเมมเบรนไมโครฟิลเตรชันมีการพัฒนาอย่างต่อเนื่อง เพื่อเพิ่มประสิทธิภาพในการกรองให้สูงขึ้น ในงานวิจัยนี้ได้ทำการประยุกต์ใช้ซอฟต์แวร์พลศาสตร์ของไหลเชิงคำนวณ FLUENT ในการจำลองกระบวนการเพื่อคำนวณค่าเพอร์มิเอตพลังค์ในเมมเบรนไมโครฟิลเตรชันที่มีช่องรูปดาวหกแฉกจำนวน 7 ช่อง นอกจากนี้ยังได้ศึกษาผลกระทบของแบบจำลองความปั่นป่วนแบบต่างๆ (Standard k-epsilon (SKE), Renormalization group k-epsilon (RNGKE), Realizable k-epsilon (RKE)) การประมาณค่าที่ผิว (First order upwind (FOU), Second order upwind (SOU), Quadratic upwind interpolation for convective kinetics (QUICK), Third order MUSCL (TOM)) และรูปทรงหน้าตัดช่อง (วงกลม, สามเหลี่ยม, สี่เหลี่ยม, ห้าเหลี่ยม, หกเหลี่ยม, เจ็ดเหลี่ยม, แปดเหลี่ยม, ดาวห้าแฉก และดาวแปดแฉก) ที่มีต่อค่าเพอร์มิเอตพลังค์ที่คำนวณได้ ผลการจำลองแสดงให้เห็นว่าเมื่อเปรียบเทียบกับผลการทดลองแล้ว แบบจำลองความปั่นป่วนชนิด RNGKE กับรูปแบบการประมาณค่าที่ผิวแบบ SOU เหมาะสมสำหรับการจำลองนี้ที่สุด เมื่อพิจารณาจากความถูกต้องของคำตอบและระยะเวลาที่ใช้สมเหตุสมผล นอกจากนี้ ช่องรูปดาวห้าแฉกแสดงค่าเพอร์มิเอตพลังค์สูงสุดเมื่อเปรียบเทียบกับรูปทรงอื่น เนื่องจากรูปทรงหน้าตัดแบบดาวห้าแฉกทำให้เกิดความเร็วในแนวแกนสูงสุดและนอมอลไลซ์ตัวเลขความดัน (normalized pressure number) สูงสุด

<b>Thesis Title</b>	Investigation of Flux Enhancement of Microfiltration Membrane by Using Computational Fluid Dynamics Technique
<b>Student</b>	Mr. Kritsana Saiyood
<b>Student ID.</b>	53611606
<b>Degree</b>	Master of Engineering
<b>Program</b>	Chemical Engineering
<b>Year</b>	2014
<b>Thesis Advisor</b>	Dr. Walairat Chandra-ambhorn
<b>Thesis Co-advisor</b>	Dr. Santi Wattananusorn

## ABSTRACT

Nowadays, filtering process with microfiltration membrane is continuously developed to enhance the filtration performance. In this work, FLUENT® CFD software was employed to simulate the permeate flux in microfiltration membrane with seven star-shape (hexagram) channels. The effects of turbulence models (standard k-epsilon (SKE), renormalization group k-epsilon (RNGKE), and realizable k-epsilon (RKE)) with different face interpolation schemes (first order upwind (FOU), second order upwind (SOU), quadratic upwind interpolation for convective kinetics (QUICK), and third order MUSCL (TOM)), and cross sectional channel shapes (circle, triangle, square, pentagon, hexagon, heptagon, octagon, pentagram and octagram) on simulated permeate flux were studied. Comparing with the experimental results from literature, the simulated results showed that among the studied models, the RNGKE turbulence model with SOU scheme was the most appropriate model for this simulation because of solution accuracy and reasonable time consumption. Furthermore, the pentagram channel exhibited the highest permeate flux as compared to the other geometries because of its cross sectional shape, which could generate the highest axial velocity and the highest normalized pressure number.

## ACKNOWLEDGEMENTS

For my success, I am very thankful to my thesis advisor and co-advisor, Dr. Walairat Chandra-Ambhorn and Dr. Santi Wattananusorn, Department of Chemical Engineering, King Mongkut's Institute of Technology Ladkrabang, for their introducing me to this interesting project, and for their helpful and deep discussion and encouraging guidance throughout the course of this work. Furthermore, I would like to thank all members of CFD's Group and my friends for their help, suggestion and warm collaborations. Last but not least, I would like to express my cordial and deep thanks to my family for their encouragement, understanding and huge support.

Mr. Kritsana Saiyood

# CONTENTS

	Page
ABSTRACT IN THAI.....	I
ABSTRACT IN ENGLISH.....	II
ACKNOWLEDGEMENTS.....	III
CONTENTS.....	IV
LIST OF TABLES.....	VII
LIST OF FIGURES.....	VIII
LIST OF ABBREVIATIONS.....	X
CHAPTER I INTRODUCTION.....	1
1.1 Background and motivation.....	1
1.2 Objectives of the research.....	2
1.3 Scopes of the research.....	2
1.4 Procedure of the research.....	2
1.5 Expected benefit.....	3
CHAPTER II THEORY AND LITERATURE REVIEW.....	4
2.1 Microfiltration membrane.....	4
2.1.1 Fouling and concentration polarization.....	5
2.1.2 Permeate flux.....	6
2.2 Computational fluid dynamics (CFD).....	7
2.2.1 CFD processing.....	7
2.2.2 Finite volume method.....	8
2.3 Governing equations.....	9
2.3.1 Mass conservation equation.....	9
2.3.2 Momentum equations.....	9
2.3.3 Energy equations.....	10
2.4 Turbulence and k-epsilon turbulence model.....	10
2.4.1 Characteristics of the turbulent flow.....	10
2.4.2 Reynolds average Navier-Stokes equations (RANS).....	11
2.4.3 k-epsilon turbulence model.....	15

# CONTENTS (Cont.)

	Page
2.4.3.1 Standard k-epsilon (SKE) .....	15
2.4.3.2 Renormalization group k-epsilon (RNGKE) .....	16
2.4.3.3 Realizable k-epsilon (RKE).....	16
2.5 Porous media condition.....	17
2.6 Separation discretization .....	19
2.7 Literature review.....	22
CHAPTER III SIMULATION.....	25
3.1 Model setup.....	25
3.1.1 Modeling of hexagram microfiltration membrane .....	25
3.1.2 Assumptions of the model .....	27
3.1.3 Governing equations of the model.....	28
3.1.4 Boundary conditions.....	28
3.1.5 Numerical methods.....	29
3.2 Investigation of grid independent solutions.....	29
3.3 Validation of the Model .....	30
3.4 Investigation of turbulence models.....	30
3.5 Simulation of different geometries of microfiltration membrane .....	30
CHAPTER IV RESULTS AND DISCUSSION.....	32
4.1 Investigation of grid independent solutions and validation of the model.....	32
4.2 Simulation.....	35
4.2.1 Effect of turbulence model on microfiltration membrane simulation result .....	35
4.2.2 Effect of scheme on microfiltration membrane simulation .....	38
4.2.3 Effects of membrane channel shape on permeate flux .....	40
CHAPTER V CONCLUSIONS AND RECOMMENDATIONS.....	46
5.1 Conclusions.....	46

## CONTENTS (Cont.)

	Page
5.1.1 Investigation of grid independent solutions and validation of the model .....	46
5.1.2 Effect of turbulence model on microfiltration membrane ...	46
5.1.3 Effect of scheme .....	46
5.1.4 Effects of membrane channel shape on permeate flux .....	46
5.2 Recommendations.....	46
REFERENCES.....	47
APPENDICES.....	49
VITA.....	60

## LIST OF TABLES

Table	Page
2.1 Model constant for standard k-epsilon model.....	15
2.2 Model constant for renormalization group k-epsilon model.....	16
2.3 Model constant for realizable k-epsilon model.....	17
4.1 The error range of permeate flux prediction at TMP 0.3 bar.....	34
4.2 The permeate flux and calculation time for different turbulence models.....	38
4.3 The predicted permeate flux for different schemes at TMP 0.3 bar.....	39
A.1 Coefficients of pressure correction equation and their values.....	52
B.1 Show the value of geometries.....	54
C.1 Comparison of turbulence models.....	55

## LIST OF FIGURES

Figure	Page
2.1 Microfiltration membranes of (a) dead-end or in-line filtration and (b) cross-flow filtration.....	4
2.2 The 3 types of the nature of the fouling.....	5
2.3 Schematic diagram of CFD processing.....	8
2.4 Typical point velocities in turbulent flow.....	11
2.5 One-dimensional control volumes.....	20
3.1 The process of experimental.....	25
3.2 Membrane microfiltration.....	26
3.3 Grid generation of calculation domain.....	27
3.4 Investigation procedure of grid independent solution.....	30
3.5 Grid generations of: (a) circle, (b) triangle, (c) square, (d) pentagon, (e) hexagon, (f) heptagon, (g) octagon, (h) pentagram, (i) hexagram, and (j) octagram.....	31
4.1 Number of axial grid (interval count 300).....	32
4.2 Grid sizes varied from: (a) 1,372,800, (b) 2,484,000, (c) 3,878,400, and (d) 5,556,000 cells.....	33
4.3 The effect of grid resolution on the simulated permeate flux at TMP 0.3 bar.....	34
4.4 Velocity contours of microfiltration membrane at TMP 0.3 bar using (a) SKE model, (b) RNGKE model, and (c) RKE model.....	35
4.5 Enlargement of velocity contours of microfiltration membrane at TMP 0.3 bar using (a) SKE model, (b) RNGKE model, and (c) RKE model.....	36
4.6 The comparison between TMP and the permeate flux.....	36
4.7 Axial velocity contours of microfiltration membrane (outlet) at TMP = 0.3 bar: (a) circle, (b) triangle, (c) square, (d) pentagon, (e) hexagon, (f) heptagon, (g) octagon, (h) pentagram, (i) hexagram, and (j) octagram.....	40
4.8 The predicted permeate flux per wet area of different TMP.....	42
4.9 The dimensionless centerline axial velocities along the dimensionless longitudinal distance for different inlet channel geometries.....	43

## LIST OF FIGURES (Cont.)

Figure	Page
4.10 The normalized pressure numbers at different cross section for different inlet channel geometries.....	44
A.1 The SIMPLE algorithm.....	53
C.1 Velocity contours of microfiltration membrane at TMP 0.4 bar using (a) SKE model, (b) RNGKE model, and (c) RKE model.....	56
C.2 Velocity contours of microfiltration membrane at TMP 0.5 bar using (a) SKE model, (b) RNGKE model, and (c) RKE model.....	56
C.3 Enlargement of velocity contours of microfiltration membrane at TMP 0.4 bar using (a) SKE model, (b) RNGKE model, and (c) RKE model.....	57
C.4 Enlargement of velocity contours of microfiltration membrane at TMP 0.5 bar using (a) SKE model, (b) RNGKE model, and (c) RKE model.....	57
C.5 Axial velocity contours of microfiltration membrane (outlet) at TMP = 0.4 bar: (a) circle, (b) triangle, (c) square, (d) pentagon, (e) hexagon, (f) heptagon, (g) octagon, (h) pentagram, (i) hexagram, and (j) octagram.....	58
C.6 Axial velocity contours of microfiltration membrane (outlet) at TMP = 0.5 bar: (a) circle, (b) triangle, (c) square, (d) pentagon, (e) hexagon, (f) heptagon, (g) octagon, (h) pentagram, (i) hexagram, and (j) octagram.....	58

## LIST OF ABBREVIATIONS

$C$	Inertial resistance factor
$D_{i,m}$	Mass diffusion coefficient for species $i$ in the mixture ( $m^2/s$ )
$E$	Total energy (J)
$k$	Turbulent kinetic energy (J/kg)
$L$	Total length of membrane in the model (m)
$\Delta n$	Membrane thickness (m)
$p$	Pressure (Pa)
$\Delta P$	Pressure drop (Pa)
$S_E$	Total energy source term
$S_i$	Species source term
$S_{Mx}, S_{My}, S_{Mz}$	Momentum source term in $x, y, z$ directions
$t$	Time (s)
$U$	Velocity vector
$u, v, w$	Velocity components in $x, y, z$ directions
$x_{tp}$	Position on the flow path around turbulence promoter
$x_{total,tp}$	Projected distance from leading edge to trailing edge along turbulence promoter
$x, y, z$	Rectangular coordinates
$\alpha$	Membrane permeability ( $m^2$ )
$\mu$	Viscosity ( $kg/m \cdot s$ )
$\rho$	Fluid density ( $kg/m^3$ )
$\tau_{xx}, \tau_{yy}, \tau_{zz}$	Normal stresses on $x$ - $x, y$ - $y, z$ - $z$ planes
$\tau_{xy}, \tau_{xz}, \tau_{yz}$	Shear stresses on $x$ - $y, x$ - $z, y$ - $z$ planes

# CHAPTER I

## INTRODUCTION

### 1.1 Background and motivation

In 1748, Antoine Nollet, a French physicist, discovered osmosis. Then, the parameters of membrane process, such as pore size, membrane structure and type of material, have been continuously developed. The membrane microfiltration is a filtration process that uses porous membrane to separate suspended particles to increase the purity of the mixture in many engineering applications. Nowadays, the permeate flux can be increased by different methods, such as gas assistant, non-circular membrane channel, baffle, etc. [1].

Since 1960s, the aerospace industry has integrated Computational Fluid Dynamics (CFD) techniques into design, R&D, and manufacturing of aircraft and jet engines. These methods have been applied to analyze the various fluid flow problems and become an important engineering tool because CFD can produce extremely large volumes of results at virtually low expense to perform parametric studies [2]. CFD is a branch of fluid mechanics that uses numerical method and algorithm to solve and to analyze momentum, heat and mass transfer in various systems. Phenomena of fluid flow are usually explained by three fundamental physical laws, including the conservation of mass, the Newton's second law of motion, and the first law of thermodynamics. CFD is very useful and spans a wide range of application areas. For example, fluid flow pattern in cyclone separator [3], reactor optimization [4], heat transfer in packed bed column [5] etc.

Regarding to benefits of CFD and requirement of increasing flux microfiltration membrane, many researchers have used CFD techniques together with experimental results to describe the phenomena of flow in microfiltration membrane [6]. In this work, the flow is assumed to be turbulent and incompressible. The effect of geometries of inlet flow has been investigated by the CFD modeling and predicted hydrodynamics parameters have been used to explain the observed results.

## 1.2 Objectives of the research

1. To study the internal flow phenomena in hexagram membrane microfiltration by using Computational Fluid Dynamics (CFD) and by comparing with the experimental data.
2. To study the influence of turbulence model on the accuracy of predicted results in hexagram membrane microfiltration.
3. To study the influence of other geometries that affect the filter performance and internal flow pattern in the microfiltration membrane to find the optimum geometry with the highest filter efficiency comparing with hexagram.

## 1.3 Scopes of the research

1. Create the three-dimensional model of hexagram multi-channel membrane microfiltration by using GAMBIT.
2. Compare the simulation results of hexagram membrane microfiltration with the experimental results.
3. Study the influence of turbulence models that affect hexagram membrane microfiltration.
4. Model the other geometries of membrane microfiltration (circle, triangle, square, pentagon, hexagon, heptagon, octagon, pentagram and octagram).
5. Compare the simulation results of hexagram membrane microfiltration with the results of the other geometries of microfiltration membrane.

## 1.4 Procedure of the research

1. Conduct literature survey and review.
2. Setup the model by GAMBIT.
3. Solve problems by using FLUENT®.
4. Compare simulation results with experiment data which reported in literature.
5. Change the other geometries of membrane microfiltration.
6. Make discussion and conclusions of simulation results.
7. Write thesis and prepare of manuscript for journal publication.

## 1.5 Expected benefits

1. Obtain knowledge and understanding about the modeling and calculation of the flow of membrane microfiltration by using CFD.
2. Obtain knowledge and understanding about the internal flow phenomena in membrane microfiltration, which leads to the optimization of internal flow membrane microfiltration.
3. Use the obtained knowledge as a guideline for improving the performance of microfiltration membrane to use in industries.

## CHAPTER II

### THEORY AND LITERATURE REVIEW

#### 2.1 Microfiltration membrane [7,8]

Microfiltration refers to filtration processes that use porous membranes to separate suspended particles with diameter between 0.1 and 10  $\mu\text{m}$ . Filtration consists of can be classified into (a) dead-end or in-line filtration and (b) cross-flow filtration as shown in Figure 2.1.

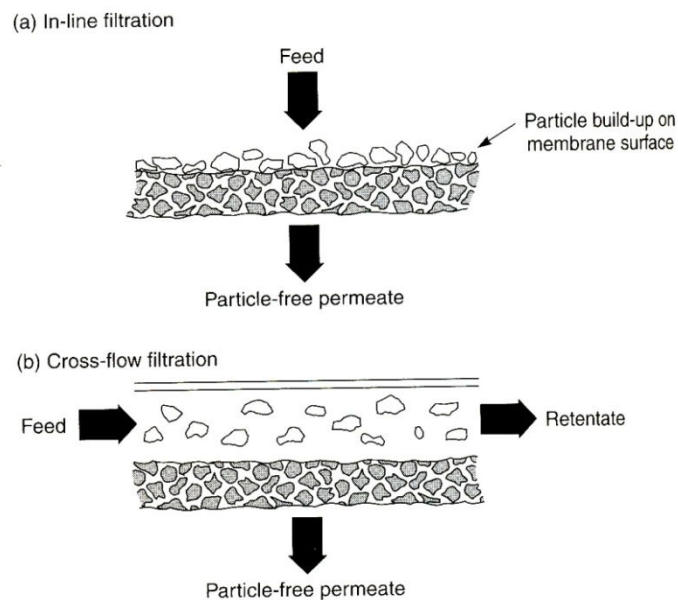


**Figure 2.1** Microfiltration membranes of (a) dead-end or in-line filtration and (b) cross-flow filtration [7]

For dead-end or in-line filtration, the fluid perpendicularly feeds over the membrane. The fluid flows through the membrane due to the pressure. Particles will accumulate on the membrane surface, causing an obstruction that must be cleaned or replaced a new membrane. For cross-flow filtration, fluid is fed across the surface of the membrane and separated into two ways, i.e., permeate and retentate (permeate: fluid is filtered and retentate: fluid that is unfiltered). The lifetime of the cross-flow filtration will be longer than the dead-end or in-line filtration because the obstruction of cross-flow filtration is less than another. Hence, cross-flow filtration is

the most commonly used in many applications and more developed by many researchers.

### 2.1.1 Fouling and concentration polarization

Concentration polarization is a phenomenon that occurs under pressure. When solute has accumulated on the surface of the membrane, cause the concentration of the solute does not pass the membrane is higher the concentration of the feed solution. So, the boundary layer at the surface of the membrane the phenomenon known as “fouling”. The fouling will reduce the efficiency of the filtration of the membrane. The fouling is divided into two types: cake layer, and pore blocking or interior pore fouling as shown in Figure 2.2. Cake layer in the fouling was arranged in layers on the top surface of the membrane. Pore blocking will occur at the opening of the aperture membrane. The interior pore fouling occurs within the pores of the membrane, marking the hold size smaller, and obstructing the flow and cleaning.

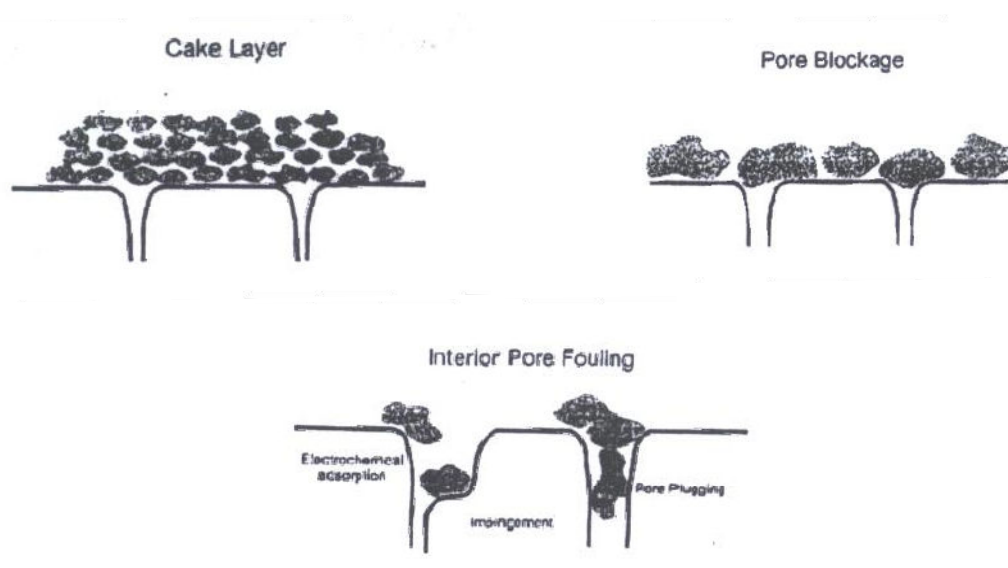


**Figure 2.2** The 3 types of the nature of the fouling [7]

The occurrence regulations of fouling and concentration polarization

1. Pretreatment for feed such as pre-filtration
2. Membrane surface modification
3. Hydrodynamic optimization of the membrane module
4. Membrane cleaning

Factors affecting the performance of a microfiltration membrane

1. Feed velocity
2. Pressure
3. Temperature

### 2.1.2 Permeate flux

Flux shows a performance of membrane filtration processes. The permeate flux, which is the volumetric flow rate of permeate through the membrane per unit area, and transmembrane pressure (TMP) are shown in Equation (1) and Equation (4), respectively.

$$J = \frac{K}{\mu} \cdot \left( \frac{\Delta P}{\Delta n} \right) \quad (1)$$

where:  $J$  is permeate flux ( $\text{m}^3/\text{m}^2 \cdot \text{s}$  or  $\text{L}/\text{m}^2 \cdot \text{h}$ )

$\mu$  is viscosity of permeate (Pa.s)

$K$  is permeability ( $\text{m}^2$ )

$$\Delta P = P_p - P_m \quad (2)$$

$P_p$  is pressure of permeate (Pa)

$P_m$  is pressure of membrane (Pa)

$$\Delta n = n_w - n_m \quad (3)$$

$n_w$  is distance from the center to the wall (m)

$n_m$  is distance from the center to the near wall (m)

And

$$\text{TMP} = \left( \frac{P_{in} + P_{out}}{2} \right) - P_p \quad (4)$$

where: TMP is pressure difference between feed and permeate stream (Pa)

$P_{in}$  is pressure of feed (Pa)

$P_{out}$  is pressure of retentate (Pa)

## 2.2 Computational Fluid Dynamics (CFD) [2, 9]

Computational Fluid Dynamics (CFD) is a branch of fluid mechanics that uses numerical technique and algorithm to solve and to analyze various flow problems. CFD becomes an important engineering tool because it can provide clear insight into many fluid flow phenomena and produces extremely large volumes of results with inexpensive operating cost. CFD is very powerful and spans a wide range of engineering application areas e.g., aerodynamics of aircraft and vehicles, hydrodynamics of ships, mixing and separation in chemical processes, etc.

### 2.2.1 CFD processing

Generally, CFD program contains three main processes, including pre-processor, solver, and post-processor.

#### Pre-processor

This step consists of the input of flow problems to a CFD program, such as definition of the computational domain, grid generation, selection of the physical and chemical phenomena, and definition of material properties.

#### Solver

Generally, there are three distinct streams of numerical solution technique, including finite difference method, finite element method, and finite volume methods. Typically, the solver performs the following steps,

- Approximation of unknown flow variables by simple function.
- Transform the Partial Differential Equations (PDEs) into algebraic equation. This step is called discretisation.
- Solution of the algebraic equations.

#### Post-processor

Post-processor contains versatile data visualization tools, such as geometry and grid display, vector plot, line and shaded contour plots, etc. CFD processing can be summarized as a diagram, shown in Figure 2.3.

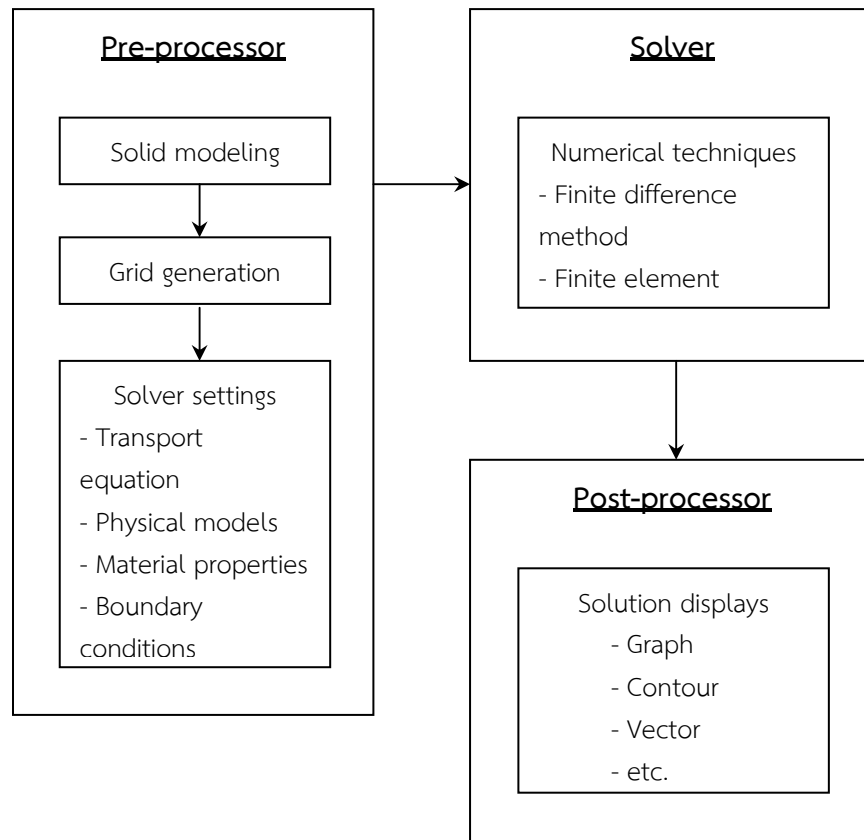


**Figure 2.3** Schematic diagram of CFD processing

### 2.2.2 Finite volume method

Finite volume method is numerical solution technique. This method was originally developed as a special finite difference formulation. Finite volume method consists of the following steps,

- Integration of fluid flow governing equations over control volume.
- Discretisation involves the substitution of a variety of finite-difference-type approximations in the integrated equation, including convection, diffusion and source terms. This step converts the integral equations into a set of algebraic equations.
- Solution of the algebraic equations by an iterative method.

## 2.3 Governing equations

The fluid problems are usually governed by three fundamental physical equations, including the conservation of mass, the Newton's second law of motion, and the first law of thermodynamics.

### 2.3.1 Mass conservation equation

The conservation of mass states that mass may be neither created nor destroyed. The mass conservation equation or continuity equation is given by

$$\frac{\partial \rho}{\partial t} + \frac{\partial}{\partial x}(\rho u) + \frac{\partial}{\partial y}(\rho v) + \frac{\partial}{\partial z}(\rho w) = 0 \quad (5)$$

or 
$$\frac{\partial \rho}{\partial t} + \nabla \cdot (\rho \mathbf{U}) = 0 \quad (6)$$

where:  $\mathbf{U}$  is the velocity vector in cartesian coordinate and given by

$$\mathbf{U} = u \mathbf{i} + v \mathbf{j} + w \mathbf{k}$$

where:  $\mathbf{i}$ ,  $\mathbf{j}$ , and  $\mathbf{k}$  are the unit vectors along x, y, and z axes, respectively.

### 2.3.2 Momentum equations

The Newton's second law of motion states that the rate of change of momentum of a system is equal to the net force acting on the system and takes place in the direction of the net force. The three momentum conservation equations are given by

x-component:

$$\rho \frac{Du}{Dt} = \frac{\partial}{\partial t}(\rho u) + \nabla \cdot (\rho u \mathbf{U}) = -\frac{\partial p}{\partial x} + \frac{\partial \tau_{xx}}{\partial x} + \frac{\partial \tau_{yx}}{\partial y} + \frac{\partial \tau_{zx}}{\partial z} + S_{Mx} \quad (7)$$

y-component:

$$\rho \frac{Dv}{Dt} = \frac{\partial}{\partial t}(\rho v) + \nabla \cdot (\rho v \mathbf{U}) = -\frac{\partial p}{\partial y} + \frac{\partial \tau_{xy}}{\partial x} + \frac{\partial \tau_{yy}}{\partial y} + \frac{\partial \tau_{zy}}{\partial z} + S_{My} \quad (8)$$

z-component:

$$\rho \frac{Dw}{Dt} = \frac{\partial}{\partial t}(\rho w) + \nabla \cdot (\rho w \mathbf{U}) = -\frac{\partial p}{\partial z} + \frac{\partial \tau_{xz}}{\partial x} + \frac{\partial \tau_{yz}}{\partial y} + \frac{\partial \tau_{zz}}{\partial z} + S_{Mz} \quad (9)$$

### 2.3.3 Energy equation

The first law of thermodynamics states that if a system is carried through a cycle, the total heat added to the system from its surroundings is proportional to the work done by the system on its surroundings. The energy equation in term of total energy ( $E$ ) is given by

$$\begin{aligned} \rho \frac{DE}{Dt} = & -\frac{\partial(up)}{\partial x} - \frac{\partial(vp)}{\partial y} - \frac{\partial(wp)}{\partial z} + \frac{\partial}{\partial x} \left( k \frac{\partial T}{\partial x} \right) + \frac{\partial}{\partial y} \left( k \frac{\partial T}{\partial y} \right) + \frac{\partial}{\partial z} \left( k \frac{\partial T}{\partial z} \right) \\ & + \frac{\partial(u\tau_{xx})}{\partial x} + \frac{\partial(u\tau_{yx})}{\partial y} + \frac{\partial(u\tau_{zx})}{\partial z} + \frac{\partial(v\tau_{xy})}{\partial x} + \frac{\partial(v\tau_{yy})}{\partial y} + \frac{\partial(v\tau_{zy})}{\partial z} \\ & + \frac{\partial(w\tau_{xz})}{\partial x} + \frac{\partial(w\tau_{yz})}{\partial y} + \frac{\partial(w\tau_{zz})}{\partial z} + S_E \end{aligned} \quad (10)$$

Equations (6)-(10) are called the compressible Navier-Stokes equations.

## 2.4 Turbulence and k-epsilon turbulence model

Fluid flow pattern, including laminar, transition, and turbulent can be identified by Reynolds number (Re). The Reynolds number can be defined as the relative importance of inertia forces and viscous forces. In experiments on fluid systems, it is observed that at values below the critical Reynolds number ( $Re_{crit}$ ), the flow is smooth and adjacent layers of fluid slide past each other in an orderly fashion. This regime is called laminar flow. At values above  $Re_{crit}$ , a complicated series of events takes place, which eventually lead to a radical change of the flow character. In the final state, the flow behavior is random and chaotic even with constant imposed boundary conditions. This regime is called turbulent flow.

### 2.4.1 Characteristics of the turbulent flow

- Highly unsteady: The velocity is a function of time. The typical point velocity measurement might exhibit the form shown in Figure 2.4.

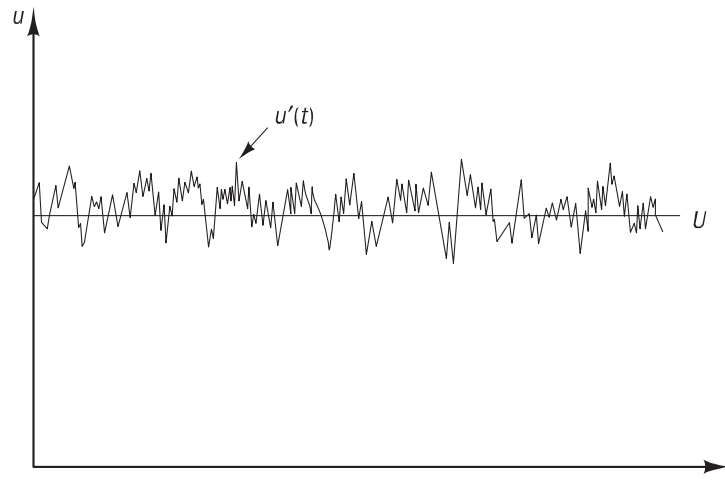


**Figure 2.4** Typical point velocities in turbulent flow [2]

- Irregularity: It is another characteristic which makes the deterministic approach to turbulence problems impossible. One should rely on statistical approach.
- Diffusivity: If the flow pattern is random, but does not exhibit spreading of velocity fluctuations through the surrounding fluid; then the flow is not turbulent. This characteristic of turbulence causes rapid mixing and increased rates of momentum, heat, and mass transfer.
- Three dimensional: Turbulence is three dimensional and rotational.
- Dissipative: The turbulent flows are always dissipative.
- Higher Reynolds number: Turbulence in the fluid flow always occurs at high Reynolds numbers.

#### 2.4.2 Reynolds average Navier-Stokes equations (RANS)

According to irregular characteristic of turbulent flow, the computations based on the complete description of all fluid particles motion are impossible. However, the computations of turbulent flow can be solved by using statistical approach. The instantaneous flow property ( $\varphi$ ) is decomposed into its time-averaged ( $\bar{\varphi}$ ) and fluctuating quantities ( $\varphi'$ ) as shown in Equation (11).

$$\varphi(t) = \bar{\varphi} + \varphi'(t) \quad (11)$$

This process is called Reynolds decomposition, which first proposed by Osborne Reynolds. The definition of time-average of flow property ( $\varphi$ ) and time-average of fluctuation property ( $\varphi'$ ) are given by

$$\bar{\varphi} = \frac{1}{\Delta t} \int_0^{\Delta t} \varphi(t) dt \quad (12)$$

$$\overline{\varphi'} = \frac{1}{\Delta t} \int_0^{\Delta t} \varphi'(t) dt \equiv 0 \quad (13)$$

Regarding to Reynolds decomposition, pressure, velocity vector, and three velocity components, including x-, y-, and z-component, can be expressed as

$$p(t) = \bar{p} + p'(t) \quad (14)$$

$$\mathbf{U}(t) = \bar{\mathbf{U}} + \mathbf{U}'(t) \quad (15)$$

$$u(t) = \bar{u} + u'(t) \quad (16)$$

$$v(t) = \bar{v} + v'(t) \quad (17)$$

$$w(t) = \bar{w} + w'(t) \quad (18)$$

The effects of fluctuations on mean flow can be investigated by replacing the Equations (14)-(18) into governing equations and applying time-average of flow property as shown in Equations (12) and (13).

The compressible continuity equation for the mean flow is given by

$$\frac{\partial \rho}{\partial t} + \frac{\partial}{\partial x}(\rho \bar{u}) + \frac{\partial}{\partial y}(\rho \bar{v}) + \frac{\partial}{\partial z}(\rho \bar{w}) = 0 \quad (19)$$

or

$$\frac{\partial \rho}{\partial t} + \nabla \cdot (\rho \bar{\mathbf{U}}) = 0 \quad (20)$$

The time-average momentum equations for compressible fluid with constant viscosity are given by

x-component:

$$\begin{aligned}
& \frac{\partial}{\partial t}(\rho\bar{u}) + \frac{\partial}{\partial x}(\rho\bar{u}^2) + \frac{\partial}{\partial y}(\rho\bar{u}\bar{v}) + \frac{\partial}{\partial z}(\rho\bar{u}\bar{w}) \\
&= -\frac{\partial\bar{p}}{\partial x} + \mu\frac{\partial^2\bar{u}}{\partial x^2} + \mu\frac{\partial^2\bar{u}}{\partial y^2} + \mu\frac{\partial^2\bar{u}}{\partial z^2} \\
&+ \left[ -\frac{\partial}{\partial x}(\rho\overline{(u')^2}) - \frac{\partial}{\partial y}(\rho\overline{u'v'}) - \frac{\partial}{\partial z}(\rho\overline{u'w'}) \right] + S_{M_x} \quad (21)
\end{aligned}$$

or

$$\begin{aligned}
& \frac{\partial}{\partial t}(\rho\bar{u}) + \nabla \cdot (\rho\bar{u}\bar{\mathbf{U}}) = -\frac{\partial\bar{p}}{\partial x} + \mu\nabla^2\bar{u} \\
&+ \left[ -\frac{\partial}{\partial x}(\rho\overline{(u')^2}) - \frac{\partial}{\partial y}(\rho\overline{u'v'}) - \frac{\partial}{\partial z}(\rho\overline{u'w'}) \right] + S_{M_x} \quad (22)
\end{aligned}$$

y-component:

$$\begin{aligned}
& \frac{\partial}{\partial t}(\rho\bar{v}) + \frac{\partial}{\partial x}(\rho\bar{v}\bar{u}) + \frac{\partial}{\partial y}(\rho\bar{v}^2) + \frac{\partial}{\partial z}(\rho\bar{v}\bar{w}) \\
&= -\frac{\partial\bar{p}}{\partial y} + \mu\frac{\partial^2\bar{v}}{\partial x^2} + \mu\frac{\partial^2\bar{v}}{\partial y^2} + \mu\frac{\partial^2\bar{v}}{\partial z^2} \\
&+ \left[ -\frac{\partial}{\partial x}(\rho\overline{u'v'}) - \frac{\partial}{\partial y}(\rho\overline{(v')^2}) - \frac{\partial}{\partial z}(\rho\overline{v'w'}) \right] + S_{M_y} \quad (23)
\end{aligned}$$

or

$$\begin{aligned}
& \frac{\partial}{\partial t}(\rho\bar{v}) + \nabla \cdot (\rho\bar{v}\bar{\mathbf{U}}) = -\frac{\partial\bar{p}}{\partial y} + \mu\nabla^2\bar{v} \\
&+ \left[ -\frac{\partial}{\partial x}(\rho\overline{u'v'}) - \frac{\partial}{\partial y}(\rho\overline{(v')^2}) - \frac{\partial}{\partial z}(\rho\overline{v'w'}) \right] + S_{M_y} \quad (24)
\end{aligned}$$

z-component:

$$\begin{aligned}
& \frac{\partial}{\partial t}(\rho\bar{w}) + \frac{\partial}{\partial x}(\rho\bar{w}\bar{u}) + \frac{\partial}{\partial y}(\rho\bar{w}\bar{v}) + \frac{\partial}{\partial z}(\rho\bar{w}^2) \\
&= -\frac{\partial\bar{p}}{\partial z} + \mu\frac{\partial^2\bar{w}}{\partial x^2} + \mu\frac{\partial^2\bar{w}}{\partial y^2} + \mu\frac{\partial^2\bar{w}}{\partial z^2} \\
&+ \left[ -\frac{\partial}{\partial x}(\rho\overline{u'w'}) - \frac{\partial}{\partial y}(\rho\overline{v'w'}) - \frac{\partial}{\partial z}(\rho\overline{(w')^2}) \right] + S_{M_z} \quad (25)
\end{aligned}$$

$$\text{or} \quad \frac{\partial}{\partial t}(\rho \bar{w}) + \nabla \cdot (\rho \bar{w} \bar{\mathbf{U}}) = -\frac{\partial \bar{p}}{\partial z} + \mu \nabla^2 \bar{w} + \left[ -\frac{\partial}{\partial x}(\rho \overline{u'w'}) - \frac{\partial}{\partial y}(\rho \overline{v'w'}) - \frac{\partial}{\partial z}(\rho \overline{w'^2}) \right] + S_{Mz} \quad (26)$$

The Equations (21)-(26) are called the Reynolds equation. There are new terms arising in Equations (21)-(26), which are associated with turbulent velocity fluctuations. These extra turbulent stresses, which describe the diffusive nature of turbulence, are called Reynolds stresses.

For convenience, the new notation of these Reynolds stresses can be expressed as

$$\bar{\tau}_{ij}^{(t)} = -\rho \overline{u'_i u'_j} = \mu_t \left( \frac{\partial \bar{u}_i}{\partial x_j} + \frac{\partial \bar{u}_j}{\partial x_i} \right) \quad (27)$$

where:  $\mu_t$  is turbulent viscosity or eddy viscosity, which usually depends strongly on position.

The relation in equation (27) was first postulated by Boussinesq in 1877. Thus, equations (22), (24), and (26) become

x-component:

$$\frac{\partial}{\partial t}(\rho \bar{u}) + \nabla \cdot (\rho \bar{u} \bar{\mathbf{U}}) = -\frac{\partial \bar{p}}{\partial x} + \mu_{eff} \nabla^2 \bar{u} + S_{Mx} \quad (28)$$

y-component:

$$\frac{\partial}{\partial t}(\rho \bar{v}) + \nabla \cdot (\rho \bar{v} \bar{\mathbf{U}}) = -\frac{\partial \bar{p}}{\partial y} + \mu_{eff} \nabla^2 \bar{v} + S_{My} \quad (29)$$

z-component:

$$\frac{\partial}{\partial t}(\rho \bar{w}) + \nabla \cdot (\rho \bar{w} \bar{\mathbf{U}}) = -\frac{\partial \bar{p}}{\partial z} + \mu_{eff} \nabla^2 \bar{w} + S_{Mz} \quad (30)$$

where:  $\mu_{eff}$  is the effective viscosity coefficient which is expressed as

$$\mu_{eff} = \mu + \mu_t \quad (31)$$

### 2.4.3 k-epsilon turbulence model

The k-epsilon model is one of the most common turbulence models, which include two extra transport equations to represent the turbulent properties of the flow. The original model was proposed by Launder and Spalding. The first transport equation is transport equation of turbulent kinetic energy (k) and the second one is transport equation of dissipation rate of turbulent kinetic energy ( $\varepsilon$ ). Nowadays, the k-epsilon model is developed by many researchers. The most common k-epsilon model in engineering application areas is standard k-epsilon (SKE), renormalization group k-epsilon (RNGKE), and realizable k-epsilon (RKE).

#### 2.4.3.1 Standard k-epsilon (SKE)

k-transport equation:

$$\frac{\partial}{\partial t}(\rho k) + \frac{\partial}{\partial x_i}(\rho k u_i) = \frac{\partial}{\partial x_j} \left[ \left( \mu + \frac{\mu_t}{\sigma_k} \right) \frac{\partial k}{\partial x_j} \right] + G_k + G_b - \rho \varepsilon - Y_M + S_k \quad (32)$$

$\varepsilon$ -transport equation:

$$\frac{\partial}{\partial t}(\rho \varepsilon) + \frac{\partial}{\partial x_i}(\rho \varepsilon u_i) = \frac{\partial}{\partial x_j} \left[ \left( \mu + \frac{\mu_t}{\sigma_\varepsilon} \right) \frac{\partial \varepsilon}{\partial x_j} \right] + C_{1\varepsilon} \frac{\varepsilon}{k} (G_k + C_{3\varepsilon} G_b) - C_{2\varepsilon} \rho \frac{\varepsilon^2}{k} + S_\varepsilon \quad (33)$$

where:  $\mu_t = \rho C_\mu \frac{k^2}{\varepsilon}$ ,  $G_k = -\overline{\rho u_i' u_j'} \frac{\partial u_j}{\partial x_i}$ ,  $G_b = \beta g_i \frac{\mu_t}{Pr_t} \frac{\partial T}{\partial x_i}$ ,  $Y_M = 2\rho \varepsilon M_t^2$ ,

$C_{3\varepsilon} = \tanh \left| \frac{y}{u} \right|$  and the model constants in these equations are shown in Table 2.1.

**Table 2.1** Model constant for standard k-epsilon model

$C_{1\varepsilon}$	$C_{2\varepsilon}$	$C_\mu$	$\sigma_k$	$\sigma_\varepsilon$
1.44	1.92	0.09	1.0	1.3

### 2.4.3.2 Renormalization group k-epsilon (RNGKE)

k-transport equation:

$$\frac{\partial}{\partial t}(\rho k) + \frac{\partial}{\partial x_j}(\rho k u_j) = \frac{\partial}{\partial x_j} \left( a_k \mu_{eff} \frac{\partial k}{\partial x_j} \right) + G_k + G_b - \rho \varepsilon - Y_M + S_k \quad (34)$$

$\varepsilon$  -transport equation:

$$\frac{\partial}{\partial t}(\rho \varepsilon) + \frac{\partial}{\partial x_j}(\rho \varepsilon u_j) = \frac{\partial}{\partial x_j} \left( a_\varepsilon \mu_{eff} \frac{\partial \varepsilon}{\partial x_j} \right) + C_{1\varepsilon} \frac{\varepsilon}{k} (G_k + C_{3\varepsilon} + G_b) - C_{2\varepsilon} \rho \frac{\varepsilon^2}{k} - R_\varepsilon + S_\varepsilon \quad (35)$$

where:  $\mu_{eff} = \rho C_\mu \frac{k^2}{\varepsilon}$ ,  $G_k = -\overline{\rho u'_i u'_j} \frac{\partial u_j}{\partial x_i}$ ,  $G_b = \beta g_i \frac{\mu_t}{Pr_t} \frac{\partial T}{\partial x_i}$ ,  $Y_M = 2\rho \varepsilon M_t^2$ ,

$C_{3\varepsilon} = \tanh \left| \frac{v}{u} \right|$  and the model constants in these equations are shown in Table 2.2.

**Table 2.2** Model constant for renormalization group k-epsilon model

$C_{1\varepsilon}$	$C_{2\varepsilon}$	$C_\mu$
1.42	1.68	0.0845

### 2.4.3.3 Realizable k-epsilon (RKE)

k-transport equation:

$$\frac{\partial}{\partial t}(\rho k) + \frac{\partial}{\partial x_j}(\rho k u_j) = \frac{\partial}{\partial x_j} \left[ \left( \mu + \frac{\mu_t}{\sigma_k} \right) \frac{\partial k}{\partial x_j} \right] + G_k + G_b - \rho \varepsilon - Y_M + S_k \quad (36)$$

$\varepsilon$  -transport equation:

$$\begin{aligned} \frac{\partial}{\partial t}(\rho \varepsilon) + \frac{\partial}{\partial x_j}(\rho \varepsilon u_j) = & \frac{\partial}{\partial x_j} \left[ \left( \mu + \frac{\mu_t}{\sigma_\varepsilon} \right) \frac{\partial \varepsilon}{\partial x_j} \right] \\ & + \rho C_{1\varepsilon} \varepsilon - \rho C_{2\varepsilon} \frac{\varepsilon^2}{k + \sqrt{v \varepsilon}} + C_{1\varepsilon} \frac{\varepsilon}{k} C_{3\varepsilon} G_b + S_\varepsilon \end{aligned} \quad (37)$$

where:  $\mu_t = \rho C_\mu \frac{k^2}{\varepsilon}$ ,  $G_k = -\overline{\rho u'_i u'_j} \frac{\partial \overline{u_j}}{\partial x_i}$ ,  $G_b = \beta g_i \frac{\mu_t}{Pr_t} \frac{\partial T}{\partial x_i}$ ,  $Y_M = 2\rho\varepsilon M_t^2$ ,

$C_{3\varepsilon} = \tanh\left|\frac{v}{u}\right| C_1 = \max\left[0.43, \frac{\eta}{\eta+5}\right]$ ,  $\eta = s \frac{k}{\varepsilon}$ ,  $s = \sqrt{2S_{ij}S_{ij}}$  and the model constants in

these equations are shown in Table 2.3.

**Table 2.3** Model constant for realizable k-epsilon model

$C_{1\varepsilon}$	$C_{2\varepsilon}$	$\sigma_k$	$\sigma_\varepsilon$
1.44	1.9	1.0	1.2

## 2.5 Porous media modeling [10]

The porous media model can be used for a wide variety of single phase and multiphase problems, including flow through packed beds, filter papers, perforated plates, flow distributors, and tube banks.

Porous media are modeled by the addition of a momentum source term to the standard fluid flow equations. The source term is composed of two parts: a viscous loss term (Darcy, the first term on the right-hand side of Equation 38), and an inertial loss term (the second term on the right-hand side of Equation 38)

$$S_i = -\left( \sum_{j=1}^3 D_{ij} \mu v_j + \sum_{j=1}^3 C_{ij} \frac{1}{2} \rho |v| v_j \right) \quad (38)$$

Where  $S_i$  is the source term for the  $i^{\text{th}}$  (x, y, or z) momentum equation,  $|v|$  is the magnitude of the velocity and  $D$  and  $C$  are prescribed matrices. This momentum sink contributes to the pressure gradient in the porous cell, creating a pressure drop that is proportional to the fluid velocity (or velocity squared) in the cell.

To recover the case of simple homogeneous porous media

$$S_i = -\left( \frac{\mu}{\alpha} v_i + C_2 \frac{1}{2} \rho |v| v_i \right) \quad (39)$$

where  $\alpha$  is the permeability and  $C_2$  is the inertial resistance factor, simply specify  $D$  and  $C$  as diagonal matrices with  $1/\alpha$  and  $C_2$ , respectively, on the diagonals (and zero for the other elements).

ANSYS FLUENT also allows the source term to be modeled as a power law of the velocity magnitude:

$$S_i = -C_0 |v|^{C_1} = -C_0 |v|^{(C_1-1)} v_i \quad (40)$$

where:  $C_0$  and  $C_1$  are user-defined empirical coefficients.

In the power-law model, the pressure drop is isotropic and the units for  $C_0$  are SI.

- Darcy's law in porous media

In laminar flows through porous media, the pressure drop is typically proportional to velocity and the constant  $C_2$  can be considered to be zero. Ignoring convective acceleration and diffusion, the porous media model then reduces to Darcy's Law:

$$\nabla p = -\frac{\mu}{\alpha} \vec{v} \quad (41)$$

The pressure drop that ANSYS FLUENT computes in each of the three (x, y, z) coordinate directions within the porous region is then

$$\Delta p_x = \sum_{j=1}^3 \frac{\mu}{\alpha_{xj}} v_j \Delta n_x \quad (42a)$$

$$\Delta p_y = \sum_{j=1}^3 \frac{\mu}{\alpha_{yj}} v_j \Delta n_y \quad (42b)$$

$$\Delta p_z = \sum_{j=1}^3 \frac{\mu}{\alpha_{zj}} v_j \Delta n_z \quad (42c)$$

Where  $1/\alpha_{ij}$  are the entries in the matrix  $D$  in Equation (38),  $v_j$  are the velocity components in the x, y, and z directions, and  $\Delta n_x$ ,  $\Delta n_y$  and  $\Delta n_z$  are the thicknesses of the medium in the x, y, and z directions.

- Inertial losses in porous media

At high flow velocities, the constant  $C_2$  in Equation (38) provides a correction for inertial losses in the porous medium. This constant can be viewed as a loss coefficient per unit length along the flow direction, thereby allowing the pressure drop to be specified as a function of dynamic head.

Modeling a perforated plate or tube bank can sometimes eliminate the permeability term and use the inertial loss term alone, yielding the following simplified form of the porous media equation:

$$\Delta p = - \sum_{j=1}^3 C_{2ij} \left( \frac{1}{2} \rho v_j |v| \right) \quad (43)$$

or when written in terms of the pressure drop in the x, y, z directions:

$$\Delta p_x \approx - \sum_{j=1}^3 C_{2xj} \Delta n_x \left( \frac{1}{2} \rho v_j |v| \right) \quad (44a)$$

$$\Delta p_y \approx - \sum_{j=1}^3 C_{2yj} \Delta n_y \left( \frac{1}{2} \rho v_j |v| \right) \quad (44b)$$

$$\Delta p_z \approx - \sum_{j=1}^3 C_{2zj} \Delta n_z \left( \frac{1}{2} \rho v_j |v| \right) \quad (44c)$$

## 2.6 Spatial discretization

Generally, Finite Volume Method, the discrete values of the scalar  $\phi$  store at cell center. However, the face values  $\phi_f$  are required for convection terms in discrete governing equations and can be interpolated by using cell center values. In this research, there are many discretization schemes in FLUENT, such as first order upwind, second order upwind, central differencing scheme, etc. In order to achieve the correct simulated results, the appropriate discretization scheme, which depends on flow situation, should be selected.

In this section, the discretization schemes of this study, including first order upwind, second order upwind, QUICK, and third order MUSCL, and other useful schemes (central differencing scheme) are explained as the following.

- First order upwind

Typically, the upwind scheme is the most commonly used discretisation scheme in a strongly convective flow (e.g. turbulent flow). For strongly convective flow, the face value should receive much stronger influencing from upwind cell than from downwind cell. This scheme takes into account the flow direction when determining the face value.

The face value  $\phi_f$  of first order upwind scheme can be illustrated by considering Figure 2.5.

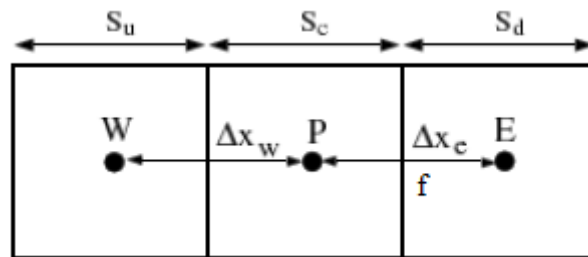


Figure 2.5 One-dimensional control volumes

The face value  $\phi_f$  is set equal to the cell center value of upstream cell as shown in Equation (45).

$$\phi_f = \phi_P \quad (45)$$

The advantages of this scheme are easy to implement and high stability in calculation. Thus, the first order upwind scheme should be adopted at start of the calculation to prevent the divergence.

- Second order upwind

The second order upwind is a higher upwind scheme. The quantities at cell faces are computed using a multidimensional linear reconstruction approach [10]. In this approach, second order accuracy is obtained at cell faces through a Taylor series expansion of the cell centered solution about the cell centroid. From Figure 2.5, the face value of this scheme can be expressed as depicted in Equation (46).

$$\phi_f = \phi_P + \left( \frac{\phi_P - \phi_W}{S_u + S_c} \right) S_c \quad (46)$$

This is a default interpolation scheme in FLUENT because of its stability and its accuracy.

- Central differencing scheme

The Central differencing scheme is another second order accurate discretization scheme. The face value of central differencing scheme can be obtained by considering Figure 2.5. The face value of this second order accurate discretization scheme is represented in Equation (47).

$$\phi_f = \frac{1}{2} \left[ \left\{ \phi_P + \left( \frac{\phi_P - \phi_W}{S_u + S_c} \right) S_c \right\} + \left\{ \phi_E + \left( \frac{\phi_E - \phi_P}{S_c + S_d} \right) S_d \right\} \right] \quad (47)$$

This scheme is more accurate when compares to first order upwind scheme. However, it leads to oscillations in the solution or divergence if the local Peclet number is larger than 2.

- QUICK

QUICK stands for the quadratic upwind interpolation for convective kinetics. This scheme is based on a weighted average of second order upwind and central interpolations of the variable. For Figure 2.5, if the flow is from left to right, the face value can be written as shown in Equation (48).

$$\phi_f = \phi_P + \frac{7}{8} \left( \frac{\phi_P - \phi_W}{S_u + S_c} \right) S_c + \frac{1}{8} \left( \frac{\phi_E - \phi_P}{S_c + S_d} \right) S_c \quad (48)$$

This scheme is a very accurate scheme, but in the regions with strong gradients, overshoot or undershoot can be occurred. This leads to stability problems in calculation.

- Third order MUSCL

This third order convection scheme was conceived from the original MUSCL (Monotone Upstream Centered Schemes for Conservation Laws) by blending a central differencing scheme and second order upwind scheme as shown in Equation (49).

$$\phi_f = \theta \phi_{f, \text{central differencing scheme}} + (1 - \theta) \phi_{f, \text{second order upwind}} \quad (49)$$

The main advantage of this scheme is applicable to arbitrary meshes unlike the QUICK scheme.

## 2.7 Literature review

Chiu et al. [6] investigated the flux enhancement in gas assisted microfiltration. The results revealed that the addition of gas can be improved the critical flux of multi-noncircular channel of ceramic membranes. In addition, Chiu et al. [11] studied the various factors that affected the flux of multi-noncircular channel of ceramic membranes. The studied parameters included cross-flow velocities, surfactant, coagulant, valency, pH and ionic strength. The flux was found to be increased with increasing the fluid velocity. The types of membrane and particle size were resulted in the flux. The decreasing in critical flux was caused by the increasing in the valency. The critical flux was increased with increasing the pH of the feed. Moreover, the increasing in critical flux was also caused by the surfactant and coagulant.

Caridis and Papathanasiou [12] discussed the process of permeate flux computation for microfiltration membranes with seven (star-shaped) channels by using numerical method. They used the Boundary Integral Method (BIM) to calculate Darcy's equation and the effective permeability ( $K_m$ ) for simulation and experiments. Besides determined  $K_m$ , this approach can be used to identify alternative designs and operating conditions in membrane modules of arbitrary geometric complexity.

Rahimi et al. [13] simulated permeate flux through microfiltration membrane on a three-dimensional domain. The Darcy's equation was adopted to calculate the flux through the surface of the membrane. They compared permeate flux obtained by computational fluid dynamics with the experimental results. There were four cell setups, including the cell without the barrier, the cell with small trapezoidal barrier,

the cell with big trapezoidal barrier, and the cell with skew barriers in two opposite rows. They used the k-epsilon turbulence model to simulate the turbulence. This simulation described the changes of pressure from the entrance to the exit on the surface membrane, which was resulted in the flow pattern in the membrane. The membrane permeate flux was caused by the mass flow rate as well as the transmembrane pressure (TMP).

Parvareh et al. [14] studied the role of fluid flow pattern and dynamic pressure on the permeate flux through a microfiltration membrane in laboratory scale by using the computational fluid dynamics (CFD). They installed the impeller in the membrane. The impeller was rotated in the clockwise and counter clockwise directions with the same angular velocities to illustrate the effect of rotation direction on permeate flux. They employed SIMPLE pressure-velocity algorithm, the standard interpolation scheme for pressure, the second order upwind discretization scheme for momentum, turbulent kinetic energy and dissipation energy to simulate the flow pattern in the membrane. According to this study, they found that the change in dynamic pressure on the membrane surface directly affected on the permeate flux. The permeate fluxes simulated by the clockwise rotation of some cases were three times larger than those obtained by the counter clockwise rotation. The higher dynamic pressure resulted in higher membrane permeate flux.

Liu et al. [15] studied fluid flow in baffle-filled membrane tubes by using the computational fluid dynamics (CFD). Through the CFD simulations, the qualitative and quantitative properties of fluid dynamics in a baffle-filled channel could be obtained, which benefited to fully understand on the effects of two types of baffles on flow pattern, behavior and feature. The convective terms were discretized by using second-order upwind scheme. According to the study, they found that the central baffle produced higher wall shear stress. Finally, the CFD could explain why the central baffle achieved higher filtration flux than the wall baffle.

Jalilvand et al. [16] used the computational fluid dynamics (CFD) to simulate cross-flow microfiltration process and fluid flow in three-dimensional domain. Two different boundary conditions were imposed at the module entrance: simple continuous fluid flow and pulsatile flow. They solved this model by the computational fluid dynamic technique using the segregated solution method and Semi-Implicit Method for Pressure Linked Equations (SIMPLE) based on finite volume

method. Standard pressure and second-order upwind discretization scheme for pressure and momentum were employed in this modeling. They found that shear force was the highest at the entrance region and then decayed along the flow direction for both continuous and pulsatile flows. It was found that pulsatile flow could be divided into two different types: sinusoidal pulse flow and step function flow in which the latter led to higher shear forces and consequently higher permeate flux.

## CHAPTER III SIMULATION

Procedures of simulation are described in this chapter. This simulation research is based on the experimental of critical flux enhancement in gas assisted microfiltration by Chiu et al. [6]. Based on our literature survey, the following simulation procedures are designed as a tentative guideline. Simulation works would be separated into 4 parts; which are (i) Model setup, (ii) Investigation of grid independent solutions, (iii) Validation of the model, (iv) Investigation of turbulence models, and (v) Simulation of different geometries of microfiltration membrane.

### 3.1 Model setup

#### 3.1.1 Modeling of hexagram microfiltration membrane

The modeling was based on the experiment conducted by Chiu et al. [6]. The process of experimental is shown in Figure 3.1.

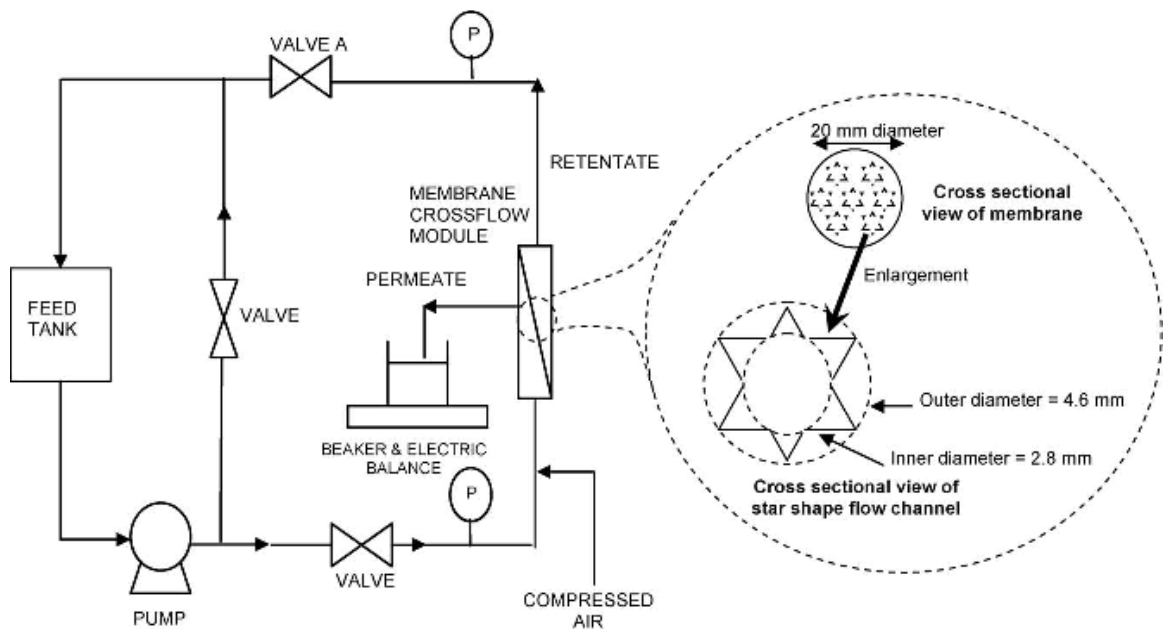


Figure 3.1 The process of experimental [6]

This experiment was conducted to separate titanium dioxide ( $\text{TiO}_2$ ) suspensions out of water. The average particle size (by volume) was found to be  $3.0 \mu\text{m}$  and pH was 7. The  $\text{TiO}_2$  suspensions were pumped from the feed tank into the membrane either as a liquid flow or as a gas-liquid concurrent two-phase flow. The microfiltration membrane used was a hexagram tubular ceramic membrane (0.3 m long, seven star channels of 4.6 mm outer diameter and 2.8 mm inner diameter) with nominal pore diameter of  $0.2 \mu\text{m}$ . The membrane filtration area was  $0.03 \text{ m}^2$  and had an equivalent hydraulic diameter of 2.3 mm. The membrane was mounted in a clear unplasticised polyvinyl chloride module which was held vertically. When fluid passed the membrane, it was separated into two lines that were permeated and retentate. The permeated was collected and weighed in a period of time in order to calculate its mass flux while retentate was returned to the feed tank.

These three-dimensional models were performed by GAMBIT. The system of a tubular membrane with seven hexagram inlet channels was described above. To simulate the membrane, the desired conditions are depicted in Figure. 3.2.

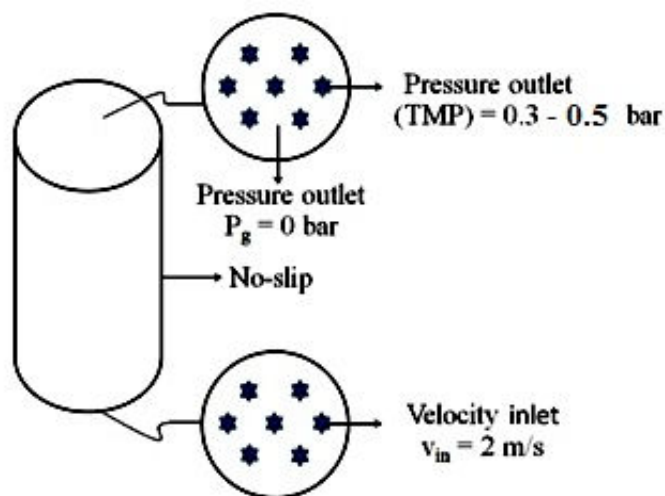


Figure 3.2 Membrane microfiltration

The example of grid generation of calculation domain of the model is shown in Figure. 3.3

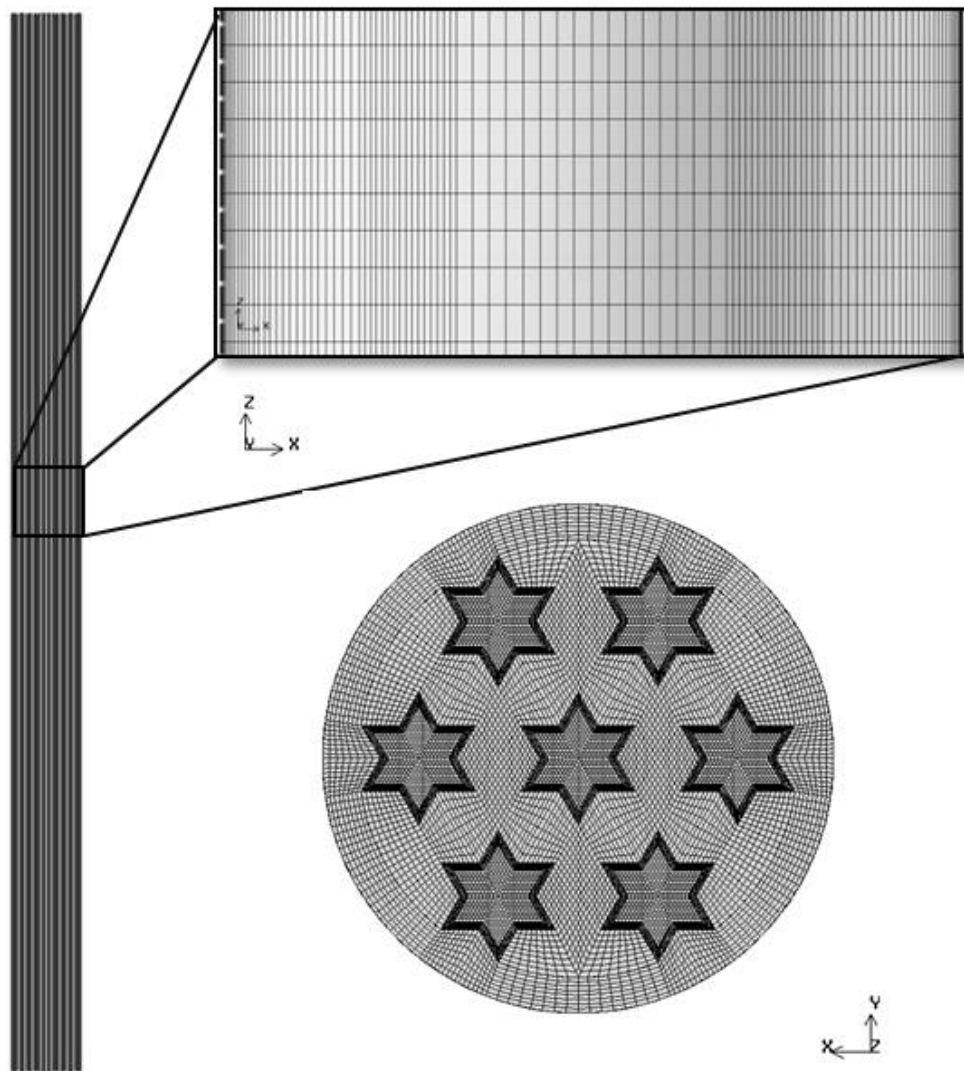


Figure 3.3 Grid generation of calculation domain

### 3.1.2 Assumptions of the model

All models were three-dimensional flow domain. The fouling formation in the system was negligible. Thus, the incompressible Newtonian fluid, i.e. water, was employed instead of titanium dioxide suspensions. The uniform flow was adopted at inlet section. The fluid motion in fluid flow channels and membrane were considered to be turbulent and laminar flow, respectively. The k-epsilon turbulence model was applied to simulate the turbulent flow in fluid channel. No-slip boundary condition was assumed at the wall.

### 3.1.3 Governing equations of the model

According to the assumptions of the model, the governing equations of the model, including continuity equation, momentum equations, can be expressed as follows previously mentioned in Chapter 2.

Continuity equation:

$$\frac{\partial \rho}{\partial t} + \frac{\partial}{\partial x}(\rho u) + \frac{\partial}{\partial y}(\rho v) + \frac{\partial}{\partial z}(\rho w) = 0 \quad (5)$$

Momentum equation in x-direction:

$$\rho \frac{Du}{Dt} = \frac{\partial}{\partial t}(\rho u) + \nabla \cdot (\rho u \mathbf{U}) = -\frac{\partial p}{\partial x} + \frac{\partial \tau_{xx}}{\partial x} + \frac{\partial \tau_{yx}}{\partial y} + \frac{\partial \tau_{zx}}{\partial z} + S_{Mx} \quad (7)$$

Momentum equation in y-direction:

$$\rho \frac{Dv}{Dt} = \frac{\partial}{\partial t}(\rho v) + \nabla \cdot (\rho v \mathbf{U}) = -\frac{\partial p}{\partial y} + \frac{\partial \tau_{xy}}{\partial x} + \frac{\partial \tau_{yy}}{\partial y} + \frac{\partial \tau_{zy}}{\partial z} + S_{My} \quad (8)$$

Momentum equation in z-direction:

$$\rho \frac{Dw}{Dt} = \frac{\partial}{\partial t}(\rho w) + \nabla \cdot (\rho w \mathbf{U}) = -\frac{\partial p}{\partial z} + \frac{\partial \tau_{xz}}{\partial x} + \frac{\partial \tau_{yz}}{\partial y} + \frac{\partial \tau_{zz}}{\partial z} + S_{Mz} \quad (9)$$

Porous media:

$$S_i = - \left( \frac{\mu}{\alpha} v_i + C \frac{1}{2} \rho |v| v_i \right) \quad (39)$$

### 3.1.4 Boundary conditions

The boundary condition for water inlet was uniform flow with velocity of 2 m/s. At the wall, no-slip boundary condition was applied. The fluid motion in hexagram channels and membrane were considered to be turbulent and laminar flow, respectively. In other words, the fluid motion in membrane was only dominated by

viscous resistance. In this work, membrane permeability ( $K_m$ ) of  $2 \times 10^{-15} \text{ m}^2$  which reported in Ref. [12] is used for the simulation.

### 3.1.5 Numerical methods

Governing equations have been solved numerically by using FLUENT® with Finite Volume Method (FVM). The computation domain is divided into a number of small cells, and the partial differential equations are integrated over each cell to obtain a set of algebraic equations. These algebraic equations were solved iteratively to obtain the field distribution of dependent variables. For this study, the pressure-velocity coupling was solved by using SIMPLE algorithm (SIMPLE algorithm are shown in the appendix A). The spatial discretization of gradient and pressure were least squares cell based and standard, respectively. Second order upwind scheme was applied to calculate momentum.

### 3.2 Investigation of grid independent solutions

The purpose of this step was to make CFD calculations that gave grid independent solutions, i.e. results that do not change when the grid is refined further. The grid independent solution can be defined as a solution that has a solution error that is within a range that can be accepted.

The procedure of grid independent solutions can be summarized as a diagram shown in Figure 3.4.

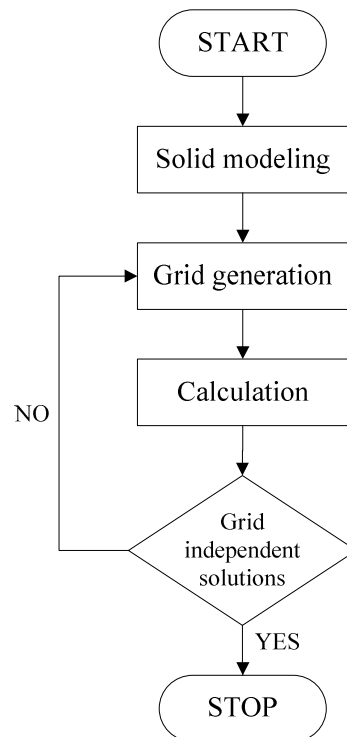


**Figure 3.4** Investigation procedure of grid independent solution

### 3.3 Validation of the model

The simulated permeate fluxes of membrane microfiltration hexagram were validated by comparing with experimental result, which reported by Chiu et al. [6].

### 3.4 Investigation of turbulence models

Three different types of k-epsilon models, including standard k-epsilon (SKE), renormalization group k-epsilon (RNGKE), and realizable k-epsilon (RKE), were used to model the turbulence. The appropriate k-epsilon model was then used to simulate the membrane microfiltration system of interest.

### 3.5 Simulation of different geometries of microfiltration membrane

In this research, the effect of the shape of membrane channel on the filtration performance was also studied and compared with the original shape (hexagram). Firstly, the channels with basic shape such as circle, triangle, square, pentagon, hexagon, heptagon, and octagon were applied to find out whether any basic shape, which should be easier to fabricate could provide better or comparable membrane

performance. Moreover, more complicate shapes adapted from hexagram such as pentagram and octagram were also applied in order to investigate the effect of characteristic of the angles on the membrane performance. Thus, for all of other geometries of membrane microfiltration, the membrane lengths were set to be 300 mm with the hydraulic diameter of 2.3 mm (hydraulic diameter calculation are shown in the appendix B) and radius of the membrane of 5 mm. Ten-studied geometries were shown in Figure 3.5.

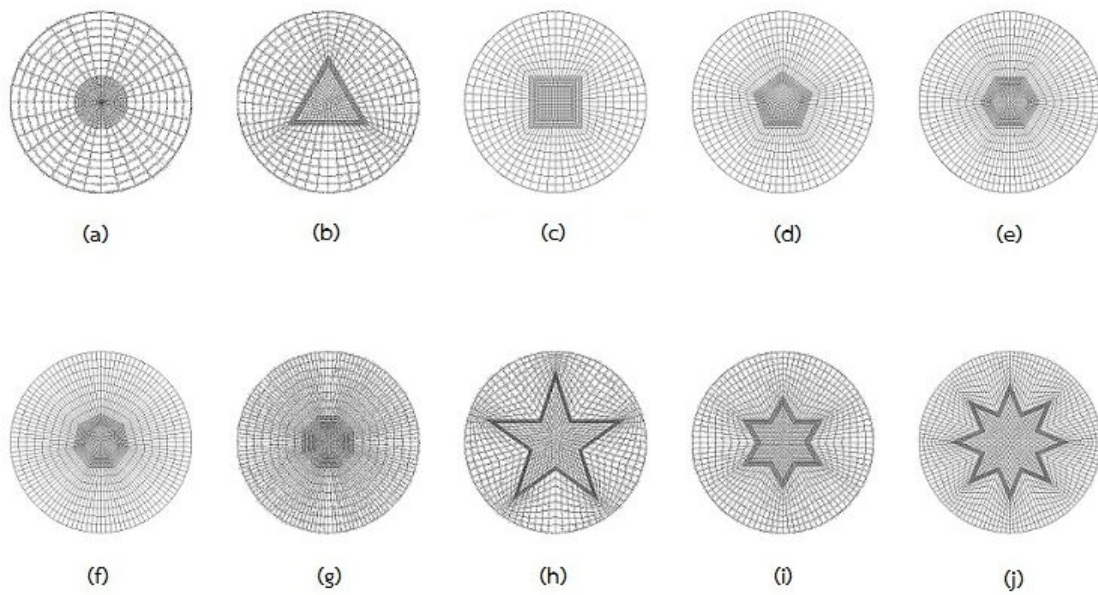


**Figure 3.5** Grid generations of (a) circle, (b) triangle, (c) square, (d) pentagon, (e) hexagon, (f) heptagon, (g) octagon, (h) pentagram, (i) hexagram, and (j) octagram

## CHAPTER IV

### RESULTS AND DISCUSSION

#### 4.1 Investigation of grid independent solutions and validation of the model

In this part, the grid generation of cross flow membrane was varied to examine grid independent solutions by using GAMBIT. Investigation of grid independent solutions is very important because grid size and resolution affect the accuracy of numerical results and calculation time. The reasonable or acceptable grid size and resolution which provide consistent simulation results with reasonable time were determined. In this section, grid sizes were changed in order to find the best quality grid. In z-direction, the whole length of the membrane was divided into 300 identical grids i.e. each step size ( $\Delta z$ ) is equal to 1 mm as shown in Figure 4.1. The pictures of all changes in grid sizes in x-y direction are shown in Figure 4.2.

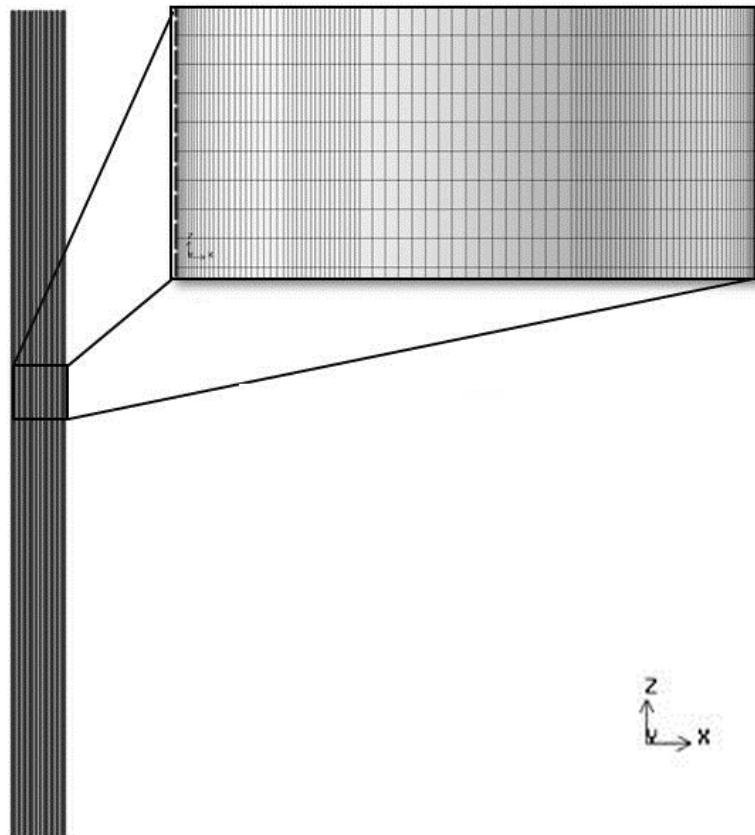
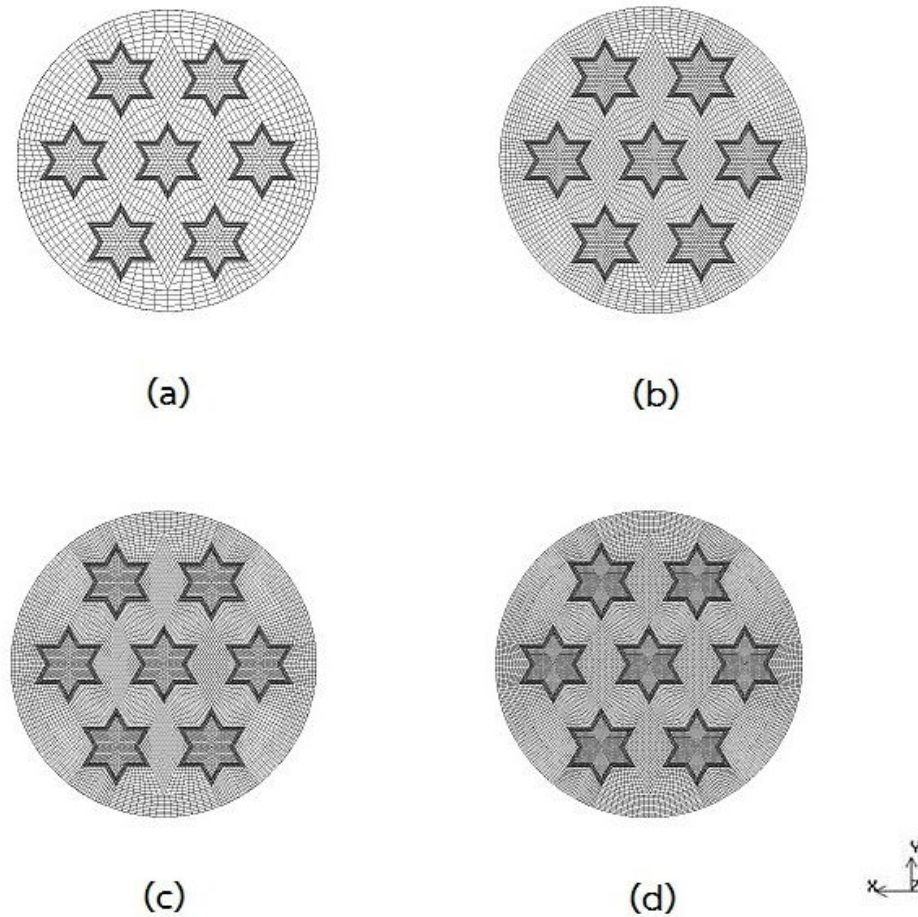


Figure 4.1 Number of axial grid (interval count 300)



**Figure 4.2** Grid sizes varied from (a) 1,372,800, (b) 2,484,000, (c) 3,878,400, and (d) 5,556,000 cells

In order to verify CFD simulation, the cross-flow microfiltration with inlet velocity of 2 m/s and transmembrane pressure (TMP) of 0.3 bar was simulated. The renormalization group k-epsilon (RNGKE) was adopted to simulate turbulence of the flow in the membrane channels. The size of membrane and geometric were identical as those depicted in Ref. [6].

The effects of grid resolution on simulation results of permeate flux and the error ranges are shown in Figure 4.3 and Table 4.1, respectively.

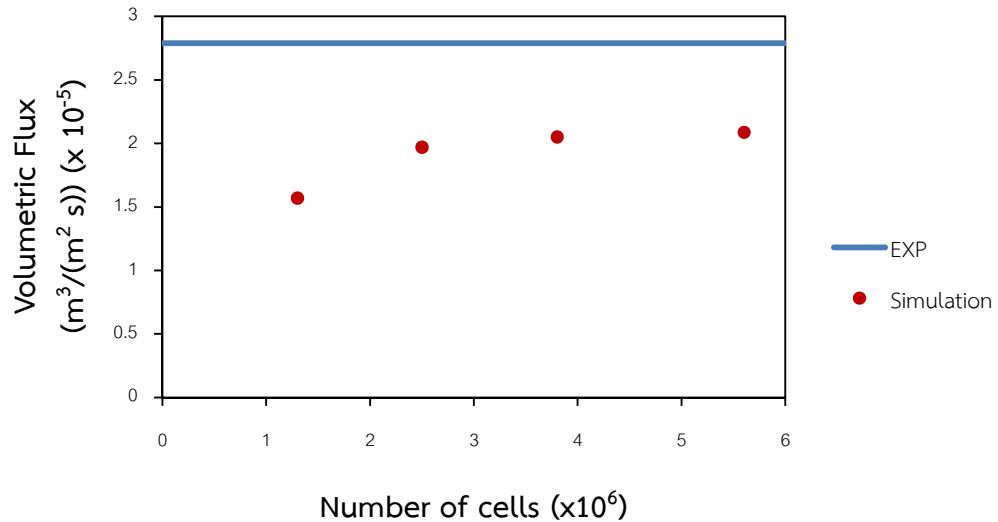


**Figure 4.3** The effect of grid resolution on the simulated permeate flux at TMP 0.3 bar

**Table 4.1** The error range of permeate flux prediction at TMP 0.3 bar

Cell	Permeate Flux (m <sup>3</sup> /(m <sup>2</sup> s))	Error	Calculation time (hr)
EXP	$2.79 \times 10^{-5}$	-	-
1,372,800	$1.57 \times 10^{-5}$	43.66%	6
2,484,000	$1.97 \times 10^{-5}$	29.46%	8
3,878,400	$2.05 \times 10^{-5}$	26.37%	12
5,556,000	$2.09 \times 10^{-5}$	25.15%	20

Figure 4.3 and Table 4.1 show the various values of permeate flux obtained from different numbers of grid. It is evident from Table 4.1 that when number of grid was increased, the error was decreased. However the increasing in number of grid also causes the calculation times to increase. In this study, the grid resolution of 3,878,400 cells should be acceptable. Upon increasing number of grid from 3,878,400 to 5,556,000 cells, we found that the errors were not significantly different but the calculation time was almost double.

Therefore, the grid resolution of 3,878,400 cells (Figure 4.2c) was used to simulate membrane microfiltration with hexagram star shape multichannel inlets later on.

## 4.2 Simulation

### 4.2.1 Effect of turbulence model on microfiltration membrane simulation results

The effect of three different types of k-epsilon model, including standard k-epsilon (SKE), renormalization group k-epsilon (RNGKE), and realizable k-epsilon (RKE) on the microfiltration membrane simulated results was studied. In this study, the cross-flow microfiltration with inlet velocity of 2 m/s, TMPs of 0.3, 0.4, and 0.5 bar and grid of 3,878,400 cells was simulated. The velocity contours at the channel outlet of this model at TMP of 0.3 bar are shown in Figure 4.4.

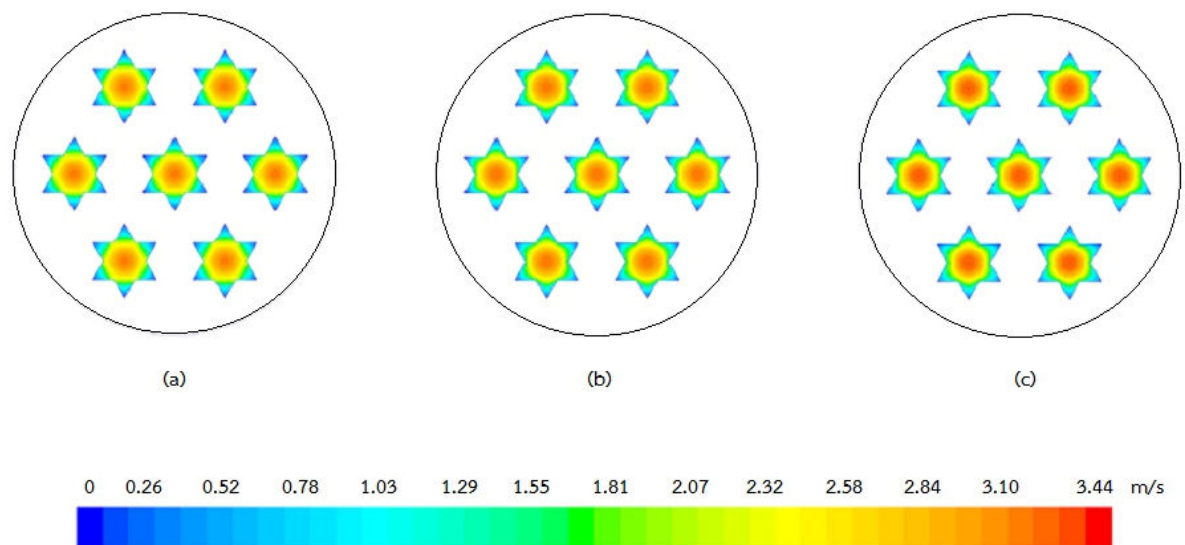


**Figure 4.4** Velocity contours of microfiltration membrane at TMP 0.3 bar using (a) SKE model, (b) RNGKE model, and (c) RKE model

It can be seen in Figure 4.4 that using different k-epsilon models provide different velocity contours as shown by different colors and shades. As in the color map in this figure, velocity varies from minimum velocity of 0 m/s, displayed in blue, to maximum velocity of 3.44 m/s, displayed in red. For each model, velocity contours of every channel are identical. The pattern of velocity contours at TMPs of 0.4 and 0.5 bar were not different when comparing with the velocity contour with respect to TMP of 0.3 bar (the velocity contours with TMPs of 0.4 and 0.5 bar are shown in the appendix D). The enlargement of velocity contours with respect to SKE, RNGKE, and RKE models is shown in Figure 4.5.

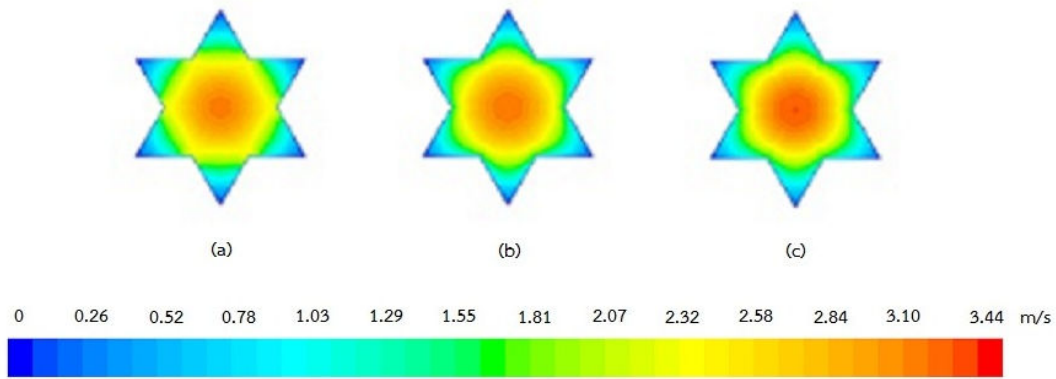


**Figure 4.5** Enlargement of velocity contours of microfiltration membrane at TMP 0.3 bar using (a) SKE model, (b) RNGKE model, and (c) RKE model

In Figure 4.5, the core flow area (displayed in red) of the contour using SKE model seems to be smaller than those of the contours using RNGKE and RKE models. Furthermore, for SKE model, the velocity at the convert angles inside the heaxgram channel is more than those predicted by RNGKE and RKE models.

This should be because SKE model does not include the effect of secondary flow in the model equations [9] (comparison of turbulence models are shown in appendix C). The secondary flow is a relatively minor flow superimposed on the primary flow. From the research of Chiu et al [6], they have identified that the internal flow through the microfiltration membrane was the secondary flow. The comparison of the enlargement of velocity contours of the three k-epsilon models showed that the core flow of the RKE model result had nature of highest speed and widest area. If core flow velocity is high, the velocity gradient will be high. Thus, the shear stress at interface of the membrane and fluid is high and the fluxes are increasing. The comparison between TMP and the permeate flux is shown in Figure 4.6.

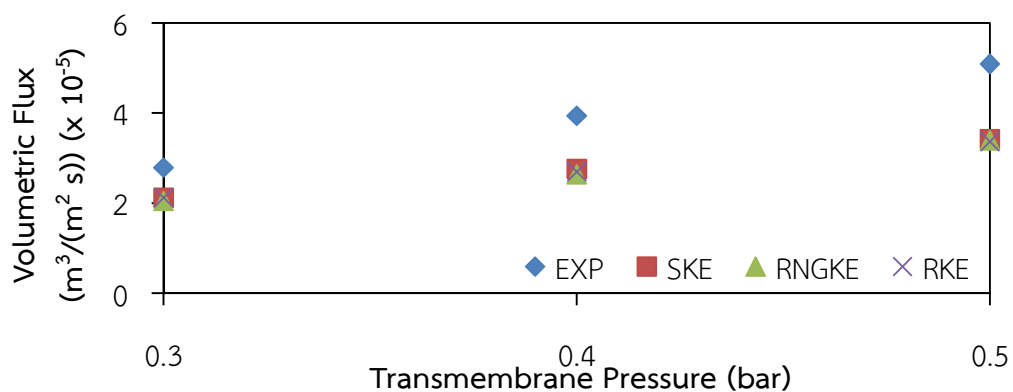


**Figure 4.6** The comparison between TMP and the permeate flux

Figure 4.6 shows the permeate fluxes obtained from the simulation of different turbulence models at different TMPs (0.3, 0.4, and 0.5 bar). It can be seen that the permeate flux tends to be in line with the experiments. The error between the experimental results and the simulated results depends on TMP. The error increases with increasing TMP. Regarding to the analytical work reported by Wattannusorn [17], the local permeate flux can be expressed as:

$$j_{(x)} = \frac{\Delta P_{(x)}}{\mu R_m}$$

where:  $\Delta P_{(x)}$  is the local transmembrane pressure (Pa)

$\mu$  is fluid viscosity (Pa.s)

$R_m$  is initial membrane resistance ( $m^2$ )

Considering the above equation, it can be seen that the permeate flux is proportional to the local transmembrane pressure. However, in present work, the transmembrane pressure is calculated by the difference between average pressure in the channel and outlet membrane pressure. Hence, the transmembrane pressure calculated by the average pressure in the channel can be firstly considered as causes of the error in permeate flux prediction. Moreover, in the real world, the value of membrane resistance is not constant, meaning that the membrane resistance depends on the distance. Finally, it can be concluded that the error in permeate flux prediction is caused by transmembrane pressure calculation and constant value of membrane resistance.

In order to obtain the suitable model for this work, the details of the simulation must be considered. The predicted permeate flux and calculation time for different turbulence models are shown in Table 4.2.

**Table 4.2** The permeate flux and calculation time for different turbulence models

TMP (bar)	Model	Permeate Flux ( $\text{m}^3/(\text{m}^2 \text{ s})$ )	Error	Calculation time (hr)
0.3	EXP	$2.79 \times 10^{-5}$	-	-
	SKE	$2.12 \times 10^{-5}$	24.01%	14
	RNGKE	$2.05 \times 10^{-5}$	26.37%	12
	RKE	$2.12 \times 10^{-5}$	24.01%	72
0.4	EXP	$3.94 \times 10^{-5}$	-	-
	SKE	$2.76 \times 10^{-5}$	29.91%	14
	RNGKE	$2.64 \times 10^{-5}$	33.05%	12
	RKE	$2.70 \times 10^{-5}$	31.38%	72
0.5	EXP	$5.09 \times 10^{-5}$	-	-
	SKE	$3.42 \times 10^{-5}$	32.85%	14
	RNGKE	$3.39 \times 10^{-5}$	33.33%	12
	RKE	$3.37 \times 10^{-5}$	33.90%	72

Table 4.2 revealed that RKE was the best model to predict the permeate flux with smallest the error. However, the calculation time of RKE was much higher than the others (5 times for SKE and 6 times for RNGKE).

In engineering applications, the accuracy and calculation time need to be compromised. As mentioned earlier, the calculation time of SKE and RNGKE were extremely less than RKE. In addition, the RNGKE was more accurate than SKE. Thus, RNGKE was the suitable model for simulation of microfiltration membrane multi-channel seven hexagram shapes.

#### 4.2.2 Effect of scheme on microfiltration membrane simulation

According to finite volume method (FVM), the interpolation of face values is required. In this simulation, the various types of momentum numerical scheme, including first order upwind (FOU), second order upwind (SOU), quadratic upwind interpolation for convective kinetics (QUICK) and third order MUSCL (TOM), were simulated to obtain the appropriate scheme for this flow situation. The results are shown in Table 4.3.

**Table 4.3** The predicted permeate flux for different schemes at TMP 0.3 bar

Model	Permeate Flux ( $\text{m}^3/(\text{m}^2 \text{ s})$ )	Error
EXP	$2.79 \times 10^{-5}$	-
FOU	$1.91 \times 10^{-5}$	31.40%
SOU	$2.05 \times 10^{-5}$	26.37%
TOM	$1.92 \times 10^{-5}$	31.18%
QUICK	$1.92 \times 10^{-5}$	31.18%

In Table 4.3, when compared to experimental data, the permeate flux obtained by SOU had least error while FOU, QUICK, and TOM provided larger errors. Therefore, SOU is the most appropriate numerical scheme for this research in comparison with other investigated schemes.

The error of four different momentum interpolation schemes can be explained by using the knowledge of physics in turbulent flow and mathematics. First, the error of SOU was lower than that of FOU because SOU scheme provided the higher order term as discussed in Section 2.7. Hence, it can be concluded that the SOU is more accurate than FOU.

In view of mathematics, the higher interpolation scheme should give more accurate solution when comparing with lower scheme. However, in present study, the error obtained by SOU (lower interpolation scheme) was lower than those obtained by two other higher schemes. As mentioned earlier in Section 2.7, the SOU scheme estimates the face value by using only the upwind cell value. In contrary, two other higher schemes compute the face value by using upwind and downwind cell value. In this case, only mathematics is not sufficient to explain the error predicted by three other higher schemes. In order to understand the error of these discretisation schemes, the physics in turbulent flow is employed.

Regarding to physics in turbulent flow, the downstream is strongly affected by upwind flow. Thus, in turbulent flow simulation, it can be implied that the face value is stronger affected by upwind cell than downwind cell. In other words, the correct estimated face value depended on upwind cell. Hence, the result obtained by SOU was more accurate than those computed by QUICK and TOM as depicted in Table 4.3.

According to these results, the optimal momentum discretisation scheme of this flow situation was SOU because it could estimate the face value by using only upwind cell value.

#### 4.2.3 Effects of membrane channel shape on permeate flux

The effect of the membrane channel shapes on the filtration performance was studied under identical hydraulic diameter, Reynolds number, and TMP. The RNGKE model with SOU scheme was adopted to simulate the cross flow membrane.

The fluid flow behaviors of these cross flow membranes are first discussed. The velocity contours of the simulated membrane for different geometries at TMP of 0.3 bar are shown in Figure 4.7.

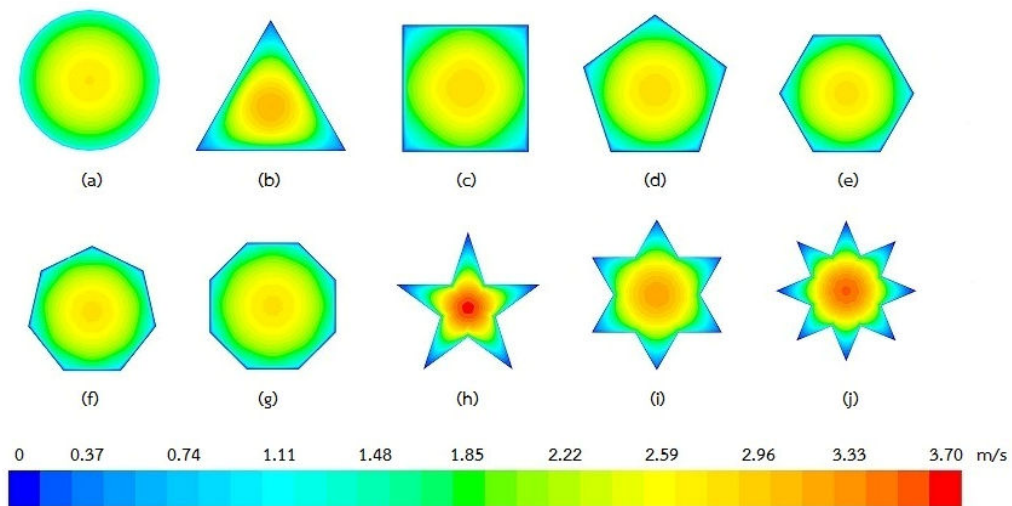


**Figure 4.7** Axial velocity contours of microfiltration membrane (outlet) at TMP = 0.3 bar:

(a) circle, (b) triangle, (c) square, (d) pentagon, (e) hexagon, (f) heptagon, (g) octagon, (h) pentagram, (i) hexagram, and (j) octagram

In the color map in Figure 4.7, velocity varies from minimum velocity of 0 m/s, displayed in blue, to maximum velocity of 3.7 m/s, displayed in red. The pattern of velocity contours of all shapes at TMPs of 0.4 and 0.5 bar were not different when comparing with the velocity contour with respect to TMP of 0.3 bar (the velocity contours with respect to TMPs of 0.4 and 0.5 bar are shown in the appendix D). The velocity contours are divided into 2 categories which, are basic shapes (circle,

triangle, square, pentagon, hexagon, heptagon, and octagon) and applied shapes (pentagram and octagram).

In the midst of basic shapes, the core flow velocity of triangle showed the maximum value. The characteristic of velocity contour of triangle shape is different when comparing with other basic shapes. The core flow shape of triangle channel is triangular because of the interior acute angles of a triangle channel. But, the core flow shapes of other basic channels seem to be circular.

For applied shapes, the core flow velocity of pentagram shape is the highest. In this study, the comparison between the internal angles of the pentagram and other shapes showed that the internal angle of pentagram shape is smaller than other shapes. According to the smallest angle of pentagram channel, the low velocity region at the corner (displayed in blue) is larger than others as depicted in Figure 4.7(h)–4.7(j). This leads to the highest core flow velocity occurred in this channel. The characteristic of boundary layer at the corner in this study may be indirectly explained in terms of the displacement thickness. The displacement thickness is a distance that occurred in wall bounded flow to satisfy the mass conservation law. These results were confirmed by the analytical study in displacement thickness reported by Wattannusorn [18]. He reported that the displacement thickness was found to increase with decreasing the angle between two flat plates. In other words, boundary layer increased with decreasing the internal angle of the channel.

Furthermore, the performances of these cross flow membranes are considered. Generally, the membrane performance can be illustrated by permeate flux. In this study, the permeate flux per wet area is conducted to indicate the membrane performance. The predicted permeate fluxes per wet area at different TMPs are shown in Figure 4.8.

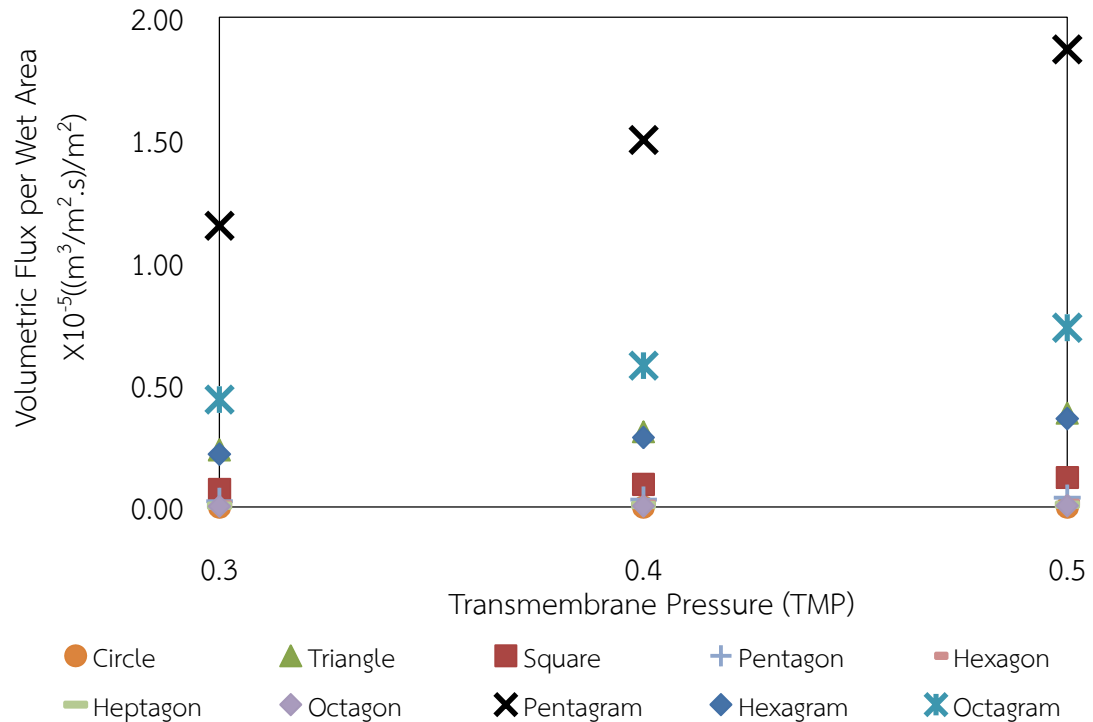


**Figure 4.8** The predicted permeate flux per wet area of different TMP

In Figure 4.8, pentagon shape provides the highest permeate fluxes per wet area followed by octagon, hexagon, triangle, square, pentagon, hexagon, heptagon, octagon and, circle, respectively. The permeate flux per wet area of a triangle shape is close to the hexagon. This should be because the internal angles of these shapes are identical (60 degree). The core flow velocity of triangle shape and hexagon were slightly different as illustrated in Figure 4.7(b) and 4.7(i).

Regarding to fundamental of fluid mechanics, the cause of momentum transfer and fluid flow are due to the velocity gradient and the pressure difference, respectively. Hence, the difference of permeate flux per wet area of all membranes can be firstly explained by considering the centerline axial velocity. The simulated centerline axial velocities of different channel geometries were represented in dimensionless form. The dimensionless centerline axial velocity can be defined as the ratio of centerline axial velocity to inlet velocity. Furthermore, the longitudinal distance of membrane channel can be written in dimensionless form as the ratio of longitudinal distance ( $z$ ) to channel length ( $L$ ). The dimensionless velocities of these membranes along the dimensionless distance are shown in Figure 4.9

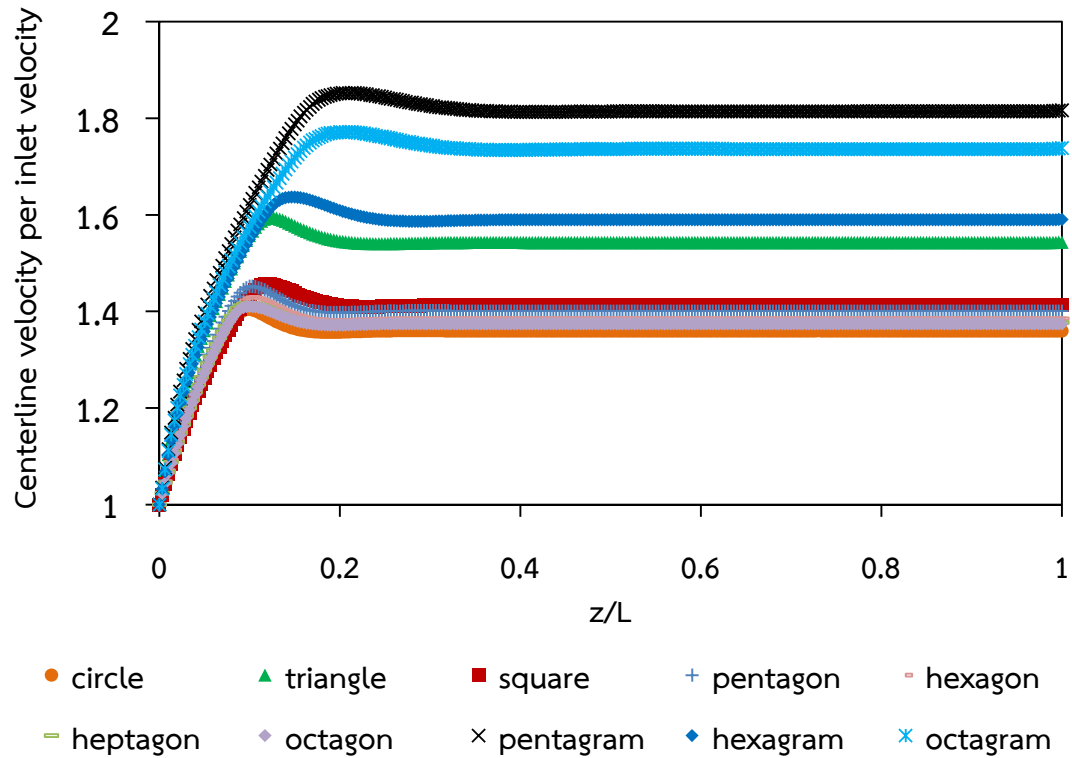


**Figure 4.9** The dimensionless centerline axial velocities along the dimensionless longitudinal distance for different inlet channel geometries

In Figure 4.9, pentagram shape shows the highest dimensionless centerline axial velocities followed by octagram, hexagram, triangle, square, pentagon, hexagon, heptagon, octagon and, circle, respectively. These results can be implied that the higher centerline axial velocity gives higher momentum transfer in transverse direction or higher shear stress. This higher shear stress also gives higher permeate flux. In other words, the higher centerline axial velocity yields higher permeate flux. The centerline axial velocity is depended on channel geometry as discuss earlier.

Only centerline axial velocity was not sufficient to explain the permeate flux per wet area. Thus, the shear stress number was also conducted to indicate the flux. Regarding to the previous work reported by Chiu et al. [6], they defined the shear stress number as the ratio of  $\rho \bar{v}^2$  to TMP. In this definition,  $\rho \bar{v}^2$  is momentum flux, which is conserved quantity. In this study, another dimensionless is defined by considering the energy, which is another conserved quantity. This new dimensionless is defined as the ratio of dynamics pressure or kinetic energy ( $1/2 \rho \bar{v}^2$ ) to TMP. This definition is called “pressure number ( $N_p$ )”. The dynamics

pressure was obtained by integrating the dynamics pressure with respect to the desired channel cross section area. In this work, the pressure numbers are presented by using normalized pressure number ( $N_p^*$ ), which is defined as

$$N_p^* \equiv \frac{N_p - N_{p, \min}}{N_{p, \max} - N_{p, \min}}$$

The normalized pressure numbers of these membranes for different cross sections are shown in Figure 4.10.

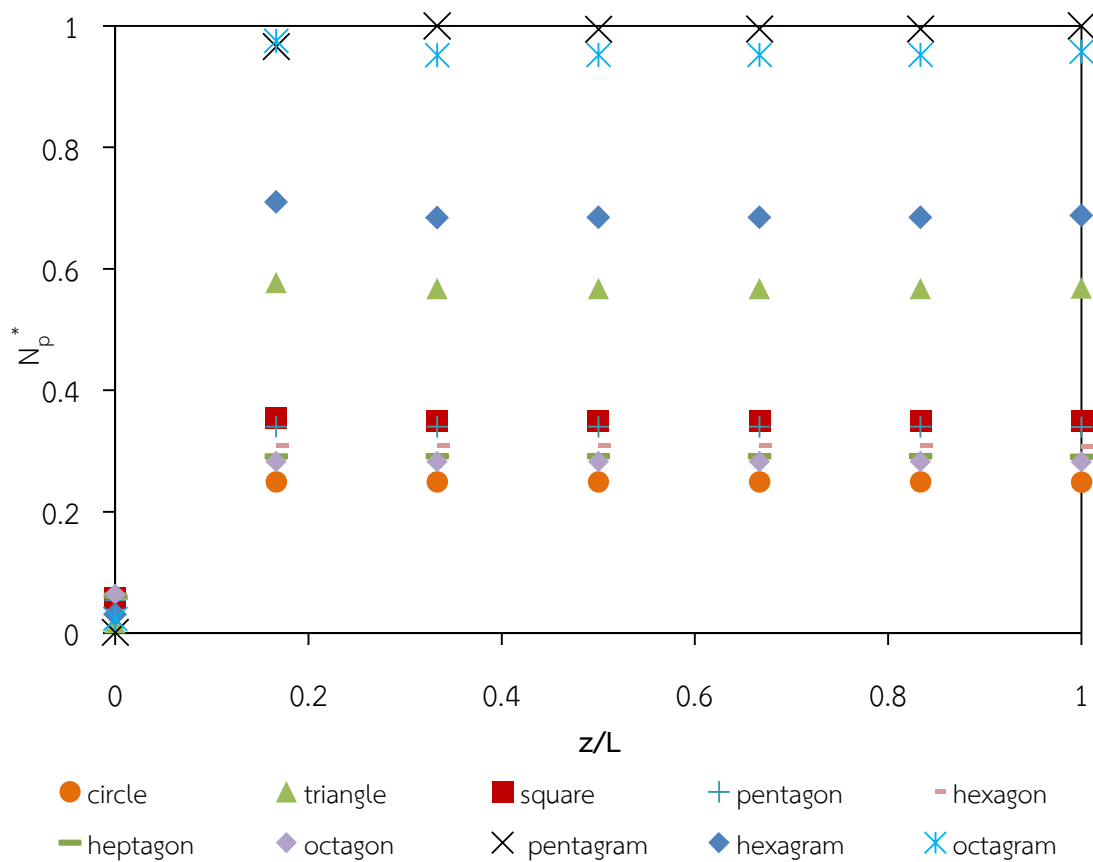


**Figure 4.10** The normalized pressure numbers at different cross section for different inlet channel geometries

In Figure 4.10, the pentagram represents the highest normalized pressure number. This higher normalized pressure number or dynamics pressure indicates the higher pressure difference between the channel and membrane outlet. The pressure difference is the cause of fluid flow. Hence, the high pressure difference makes fluid

flow through the membrane easily. In other words, the higher fluid flow through the membrane is due to the higher kinetic energy (normalized pressure number) in the channel. According to the definition of normalized pressure number, the normalized pressure number corresponds to the velocity. The high velocity field gives high normalized pressure number. As mention above, the velocity field is depended on channel cross sectional shape. So, the normalized pressure number is also depended on the channel shape.

According to these simulated results, it can be concluded that the highest permeate flux per wet area is occurred in pentagram because of its cross sectional shape, which generates the highest axial velocity and the highest normalized pressure number.

# CHAPTER V

## CONCLUSIONS AND RECOMMENDATIONS

### 5.1 Conclusions

#### 5.1.1 Investigation of grid independent solutions and validation of the model

Number of grid of 3,878,400 cells was acceptable for simulating microfiltration membrane with seven star shape channels because the error was not significantly decreased when increasing the number of grids and the calculation time was acceptable.

#### 5.1.2 Effect of turbulence model on microfiltration membrane

In this study, RNG k-epsilon model was the most appropriate model for the simulation of microfiltration membrane with seven star shape channels.

#### 5.1.3 Effect of scheme

The simulation showed that SOU provided the best calculation results in comparison with other models studied in this work.

#### 5.1.4 Effects of membrane channel shape on permeate flux

In this study, pentagram provided the highest permeate flux when comparing with the other geometries (circle, triangle, square, pentagon, hexagon, heptagon, octagon, hexagram, and octagram).

### 5.2 Recommendations

In the simulation process, effect of solid particles on the phenomenon of filtration should be studied. This will make the simulation results more accurate.

## REFERENCES

- [1] Water Environment Federation. 2006. **Membrane Systems for Wastewater Treatment** : McGraw-Hill.
- [2] Versteeg, H. K., and Malalasekera, W. 1995. **An introduction to computational fluid dynamics the finite volume method**. Malaysia : Prentice Hall.
- [3] Kaya, F., and Karagoz, I. Numerical investigation of performance characteristics of a cyclone prolonged with a dipleg. *Chemical Engineering Journal* 151 (2009) : 39-45.
- [4] Reuge, N., Bacsa, R., Serp, P., and Caussat, B. Chemical Vapor Synthesis of Zinc Oxide Nanoparticles: Experimental and preliminary modeling studies. *Journal of Physical Chemistry C* 113 (2009) : 19845-19852.
- [5] Nijemeisland, M., and Dixon, A. G. Comparison of CFD simulations to experiment for convective heat transfer in a gas–solid fixed bed. *Chemical Engineering Journal* 82 (2001) : 231-246.
- [6] T.Y. Chiu, and A.E. James, Critical flux enhancement in gas assisted microfiltration. *Journal of Membrane Science* 281 (2006) : 274–280.
- [7] Baker R. W.. 2004. **Membrane Technology and Applications**. England : Wiley.
- [8] ชันทอง สุนทรธรรมา. 2547. **เทคโนโลยีการแยกด้วยเมมเบรน (Membrane Separation Technology)**. กรุงเทพฯ : โรงพิมพ์แห่งจุฬาลงกรณ์มหาวิทยาลัย.
- [9] เอกราช บำรุงไทยชัยชาญ. 2556. **พื้นฐานพลศาสตร์ของไหลเชิงคำนวณ**. กรุงเทพฯ : ห้องปฏิบัติการพลศาสตร์ของไหลเชิงคำนวณ สาขาวิชาวิศวกรรมเคมี คณะวิศวกรรมศาสตร์ สถาบันเทคโนโลยีพระจอมเกล้าเจ้าคุณทหารลาดกระบัง.
- [10] ANSYS, Inc.. 2008. **ANSYS FLUENT 12.0 Theories' Guide**.

## REFERENCES (Cont.)

- [11] T.Y. Chiu, and A.E. James, Critical flux determination of non-circular multi-channel ceramic membranes using  $\text{TiO}_2$  suspensions, *Journal of Membrane Science*, 254 (2005) : 295–301.
- [12] Caridis KA, and Papathanasiou TD, Effective Permeability of Multichannel Cross-Flow Filtration Membranes from Permeate Flux Measurements Using the Boundary Integral Method. *Journal of Chemical Engineering of Japan* 30 (1997) : 839-845.
- [13] M. Rahimi, S.S. Madaeni, K. Abbasi, CFD modeling of permeate flux in cross-flow microfiltration membrane, *Journal of Membrane Science*, 255 (2005) : 23–31.
- [14] A. Parvareh, M. Rahimi, S. S. Madaeni and A. A. Alsairafi, Experimental and CFD Study on the Role of Fluid Flow Pattern on Membrane Permeate Flux, *Chinese Journal of Chemical Engineering*, 19 (2011) : 18-25.
- [15] Yuanfa Liu, Gaohong He, Xudong Liu, Gongkui Xiao, and Baojun Li, CFD simulations of turbulent flow in baffle-filled membrane tubes, *Separation and Purification Technology*, 67 (2009) : 14–20.
- [16] Zohreh Jalilvand, Farzin Zokaee Ashtiani, Amir Fouladitajar, and HamidRezaei, Computational fluid dynamics modeling and experimental study of continuous and pulsatile flow in flat sheet microfiltration membranes, *Journal of Membrane Science*, 450 (2014) : 207–214.
- [17] S. Wattananusorn, Determination of Membrane Resistance for Cross-Flow Microfiltration in a Rectangular Module including Back-Flow, *Journal of Process Mechanical Engineering*, 222 (2008) : 75–77.
- [18] S. Wattananusorn, Interference of laminar flow on displacement thickness in a streamwise corner, *Journal of power and energy*, 218 (2004) : 51-53.

## APPENDICES

## APPENDIX A

### SIMPLE ALGORITHM

SIMPLE stands for Semi Implicit Method for Pressure-linked Equations. This algorithm was introduced by Patankar and Spalding (1972) [2]. This method can be demonstrated by two-dimensional laminar steady flow equations in Cartesian co-ordinates.

$$a_{i,j}u_{i,j} = \sum a_{nb}u_{nb} + (p_{i-1,j} - p_{i,j})A_{i,j} + b_{i,j} \quad (\text{A-1})$$

$$a_{i,j}v_{i,j} = \sum a_{nb}v_{nb} + (p_{i,j-1} - p_{i,j})A_{i,j} + b_{i,j} \quad (\text{A-2})$$

First, the pressure field  $p^*$  (guessed pressure) is guessed. Then, substituting  $p^*$  into Equations (A-1) and (A-2) yields  $u^*$  and  $v^*$  as follows

$$a_{i,j}u_{i,j}^* = \sum a_{nb}u_{nb}^* + (p_{i-1,j}^* - p_{i,j}^*)A_{i,j} + b_{i,j} \quad (\text{A-3})$$

$$a_{i,j}v_{i,j}^* = \sum a_{nb}v_{nb}^* + (p_{i,j-1}^* - p_{i,j}^*)A_{i,j} + b_{i,j} \quad (\text{A-4})$$

Then, the pressure correction and velocities correction can be defined as follows.

$$p' = p - p^* \quad (\text{A-5a})$$

$$u' = u - u^* \quad (\text{A-5b})$$

$$v' = v - v^* \quad (\text{A-5c})$$

Subtracting Equations (A-3) and (A-4) from Equations (A-1) and (A-2), respectively. Then, use the correction formula as shown in Equations (C-5a)-(C-5c) to yield Equations (A-6) and (A-7), respectively.

$$a_{i,j}u'_{i,j} = \sum a_{nb}u'_{nb} + (p'_{i-1,j} - p'_{i,j})A_{i,j} \quad (\text{A-6})$$

$$a_{i,j}v'_{i,j} = \sum a_{nb}v'_{nb} + (p'_{i,j-1} - p'_{i,j})A_{i,j} \quad (\text{A-7})$$

Approximating Equations (A-6) and (A-7) by eliminate  $\sum a_{nb} u'_{nb}$  and  $\sum a_{nb} v'_{nb}$ . Equations (A-6) and (A-7) become

$$u'_{i,j} = d_{i,j} (p'_{i-1,j} - p'_{i,j}) \quad (\text{A-8})$$

$$v'_{i,j} = d_{i,j} (p'_{i,j-1} - p'_{i,j}) \quad (\text{A-9})$$

where:  $d_{i,j} = \frac{A_{i,j}}{a_{i,j}}$  and  $d_{i,j} = \frac{A_{i,j}}{a_{i,j}}$

Substituting equations (A-8) and (A-9) into equations (A-5b) and (A-5c), respectively. Then, rearrange the results to yield equations (A-10) and (A-11).

$$u_{i,j} = u_{i,j}^* + d_{i,j} (p'_{i-1,j} - p'_{i,j}) \quad (\text{A-10})$$

$$v_{i,j} = v_{i,j}^* + d_{i,j} (p'_{i,j-1} - p'_{i,j}) \quad (\text{A-11})$$

Similar expressions exist for  $u_{i+1,j}$  and  $v_{i,j+1}$ :

$$u_{i+1,j} = u_{i+1,j}^* + d_{i+1,j} (p'_{i,j} - p'_{i+1,j}) \quad (\text{A-12})$$

$$v_{i,j+1} = v_{i,j+1}^* + d_{i,j+1} (p'_{i,j} - p'_{i,j+1}) \quad (\text{A-13})$$

where:  $d_{i+1,j} = \frac{A_{i+1,j}}{a_{i+1,j}}$  and  $d_{i,j+1} = \frac{A_{i,j+1}}{a_{i,j+1}}$

The velocity field will satisfy continuity equation. The discretised continuity equation is given by

$$((\rho u A)_{i+1,j} - (\rho u A)_{i,j}) + ((\rho v A)_{i,j+1} - (\rho v A)_{i,j}) = 0 \quad (\text{A-14})$$

Substituting the corrected velocity into equation (A-14) yields the pressure correction equation.

$$a_{i,j} p'_{i,j} = a_{i+1,j} p'_{i+1,j} + a_{i-1,j} p'_{i-1,j} + a_{i,j+1} p'_{i,j+1} + a_{i,j-1} p'_{i,j-1} + b'_{i,j} \quad (\text{A-15})$$

where:  $a_{i,j} = a_{i+1,j} + a_{i-1,j} + a_{i,j+1} + a_{i,j-1}$  and the coefficients are given in Table A.1.

**Table A.1** Coefficients of pressure correction equation and their values

Coefficient	Value
$a_{I+1,J}$	$(\rho dA)_{i+1,J}$
$a_{I-1,J}$	$(\rho dA)_{i,J}$
$a_{I,J+1}$	$(\rho dA)_{I,j+1}$
$a_{i,J-1}$	$(\rho dA)_{I,j}$
$b'_{I,J}$	$(\rho u^* A)_{i,J} - (\rho u^* A)_{i+1,J} + (\rho v^* A)_{I,j} - (\rho v^* A)_{I,j+1}$

The source term  $b'$  is the mass imbalance which arising from the incorrect velocity field  $u^*$  and  $v^*$ . By solving equation (A-15), the correction pressure ( $p'$ ) can be obtained at all points. Then, the correct pressure and correct velocities can be obtained by solving equations (A-5a) and (A-10)-(A-13), respectively.

The earlier approximation does not affect the final solution because the correction pressure and correction velocities will be zero in converged solution giving

$$p^* = p, u^* = u \text{ and } v^* = v$$

The pressure correction is susceptible to divergence unless some under-relaxation is used during the iterative process and new, improved, pressure  $p^{new}$  are obtained with

$$p^{new} = p^* + \alpha_p p' \tag{A-16}$$

where:  $\alpha_p$  is the pressure under-relaxation factor.

A correct choice of under-relaxation factor ( $\alpha$ ) is essential for cost-effective simulations. Too large value of  $\alpha$  may lead to divergent iterative solutions and a value which is too small will cause extremely slow convergence. Unfortunately, the values of under-relaxation factors are flow dependent and must

be sought on a case-by-case basis. The procedure of SIMPLE algorithm is shown in Figure A.1.

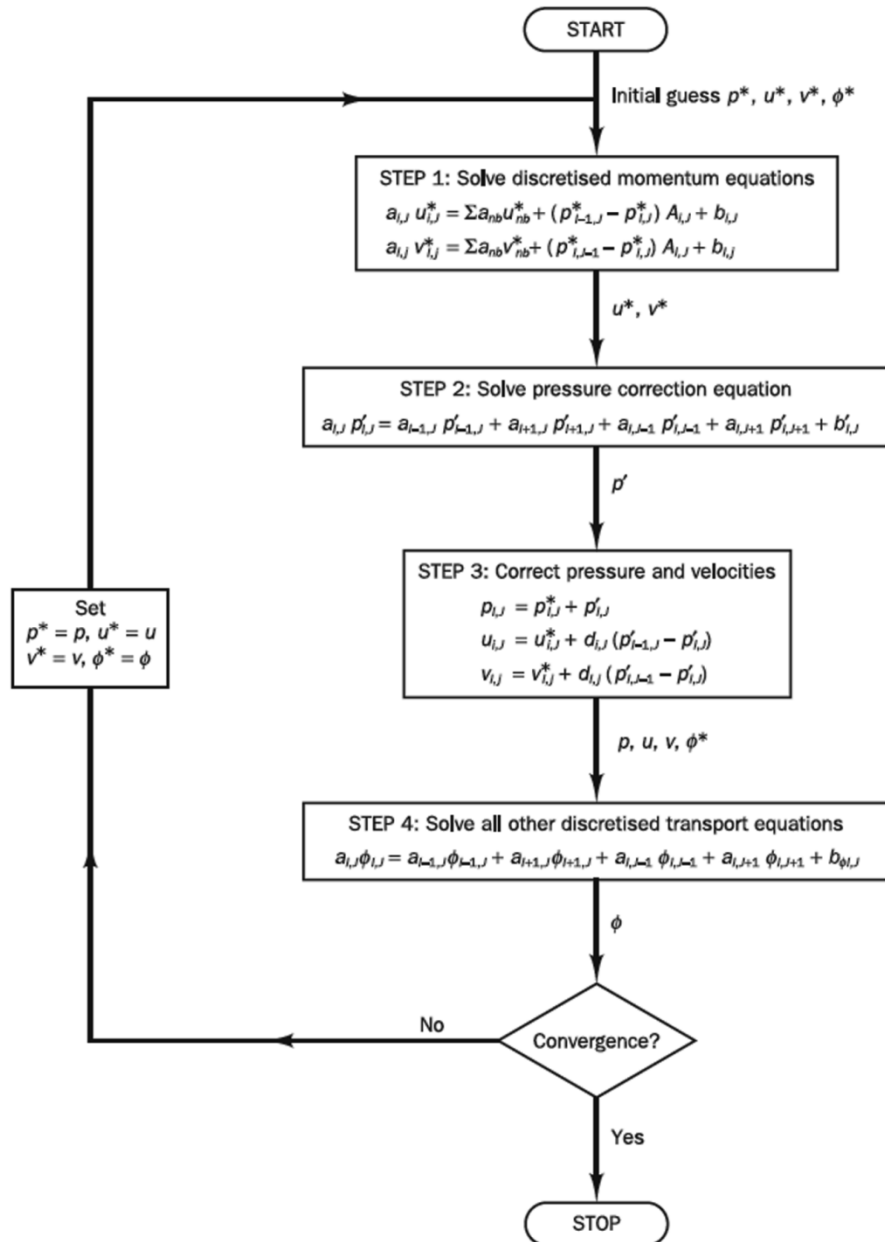


Figure A.1 The SIMPLE algorithm

## APPENDIX B

### HYDRAULIC DIAMETER CALCULATION

The hydraulic diameter,  $D_H$ , is commonly used term when handling flow in noncircular tubes or channels. The hydraulic diameter can be defined as

$$D_H = \frac{4A}{P} \quad (B-1)$$

where: A is the cross sectional area ( $m^2$ )

P is the wetted perimeter of the cross-section (m)

In this research, hydraulic diameter of the geometries equal to 0.0023 m and can be calculated from equation B-1. The cross sectional area and wetted perimeter of the cross-section for different geometries are shown in Table B.1.

**Table B.1** Show the value of geometries

Geometries	cross sectional area $\times 10^{-3} (m^2)$	wetted perimeter of the cross-section $\times 10^{-3} (m)$
Circle	4.15	7.23
Triangle	6.87	11.95
Square	5.29	9.20
Pentagon	4.81	8.36
Hexagon	4.58	7.97
Heptagon	4.46	7.75
Octagon	4.44	7.67
Pentagram	15.55	27.04
Hexagram	9.16	15.93
Octagram	14.96	26.02

## APPENDIX C

### COMPARISON OF K-EPSILON TURBULENCE MODELS

There are many types of turbulence model, such as mixing length, Spalart-Allmaras, k-epsilon, k-omega, etc. Among of these turbulence models, k-epsilon is the most widely used turbulence model because it is robust, economical, and reasonably accurate. The k-epsilon model is firstly proposed by Launder and Spalding. This turbulence model is adopted to predict the various fluid flow phenomena and shows the reasonable results. Hence, the k-epsilon turbulence model is developed or modified by many researchers to correct and improve its predicted results. Commonly, there are three types of k-epsilon model, including standard k-epsilon, renormalization group k-epsilon, and realizable k-epsilon. These k-epsilon models are developed to achieve the accurate results in different flow situations. The suitable situations of these models and the advantages can be illustrated in Table C.1

**Table C.1** Comparison of turbulence models

Model	Description
Standard k-epsilon	It is the most widely used model. It is not recommended for highly swirling flows, round jets, or for flows with strong flow separation.
RNG k-epsilon	Good for moderately complex behavior like jet impingement, separating flows, swirling flows, and secondary flows.
Realizable k-epsilon	It correctly predicts the flow in round jets. It is well suited for swirling flows and flows involving separation

APPENDIX D  
THE VELOCITY CONTOURS OF VARIOUS TMPs

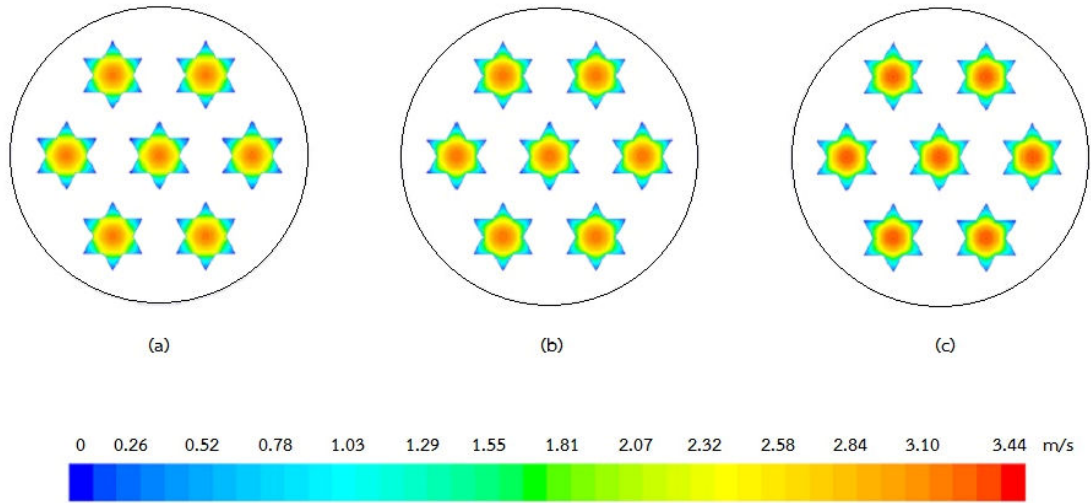


Figure C.1 Velocity contours of microfiltration membrane at TMP 0.4 bar using (a) SKE model, (b) RNGKE model, and (c) RKE model

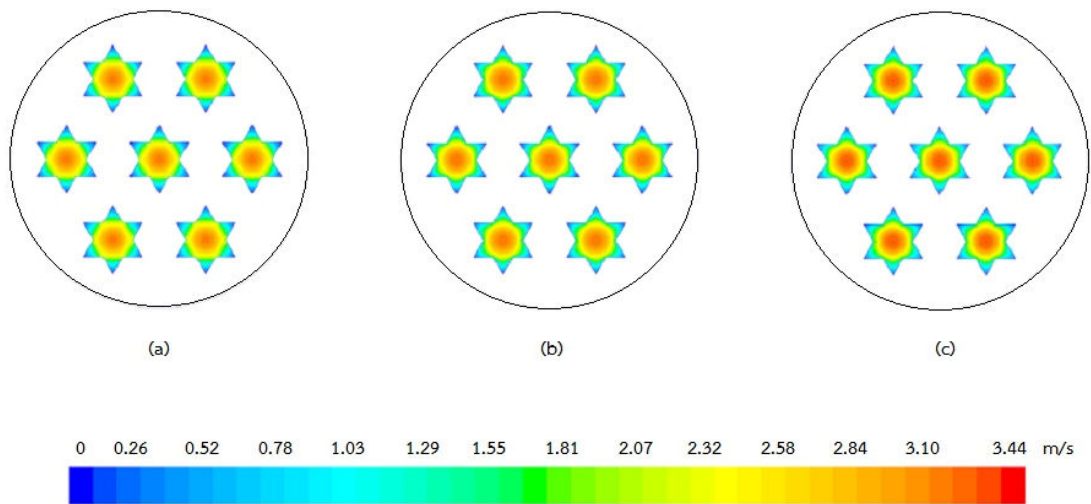
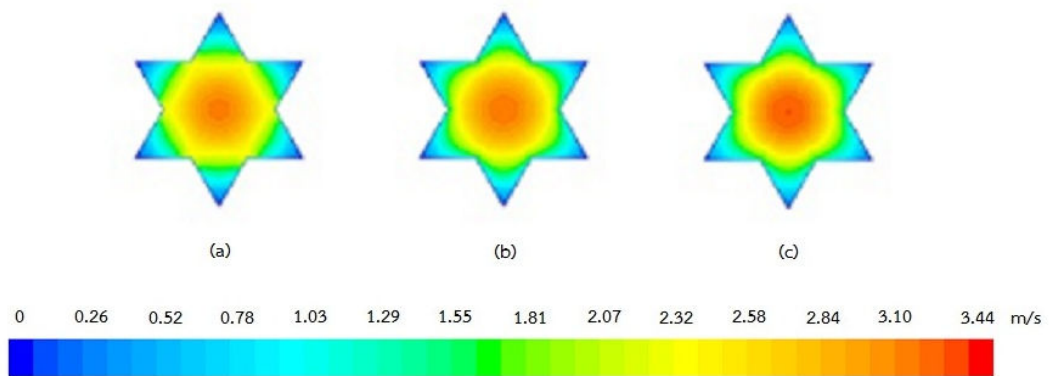
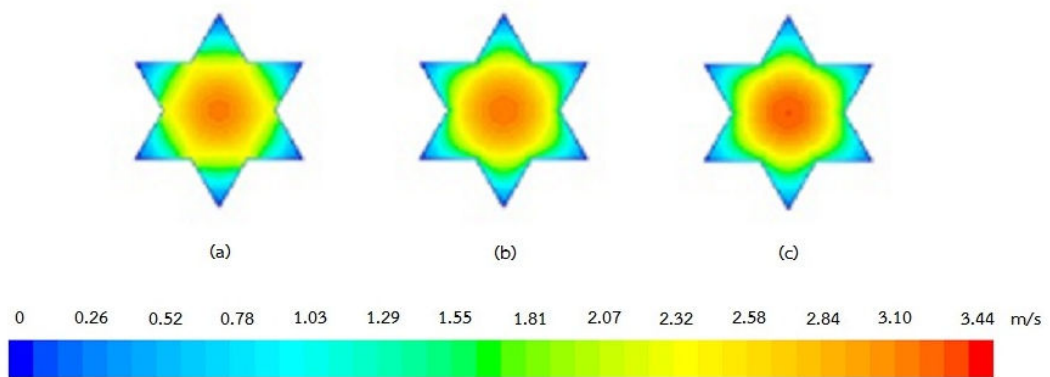


Figure C.2 Velocity contours of microfiltration membrane at TMP 0.5 bar using (a) SKE model, (b) RNGKE model, and (c) RKE model



**Figure C.3** Enlargement of velocity contours of microfiltration membrane at TMP 0.4 bar using (a) SKE model, (b) RNGKE model, and (c) RKE model



**Figure C.4** Enlargement of velocity contours of microfiltration membrane at TMP 0.5 bar using (a) SKE model, (b) RNGKE model, and (c) RKE model

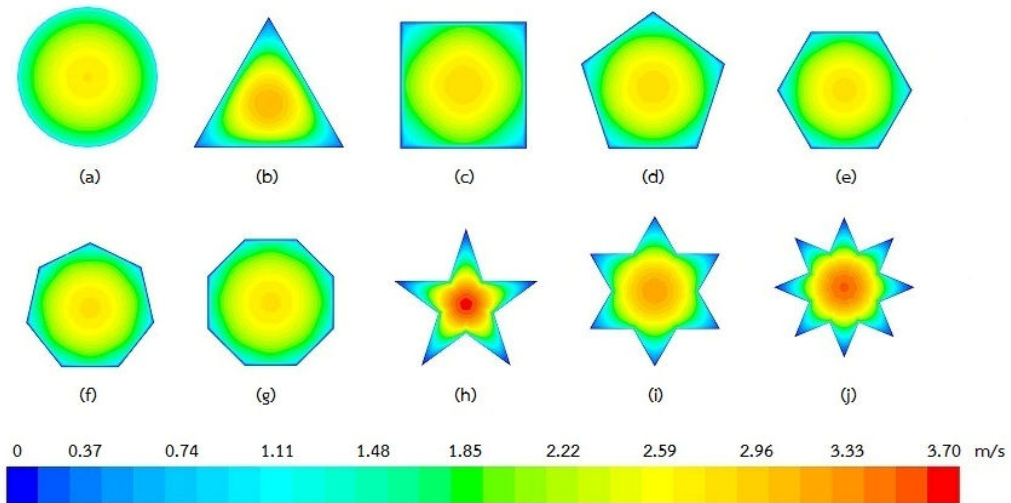


**Figure C.5** Axial velocity contours of microfiltration membrane (outlet) at TMP = 0.4 bar: (a) circle, (b) triangle, (c) square, (d) pentagon, (e) hexagon, (f) heptagon, (g) octagon, (h) pentagram, (i) hexagram, and (j) octagram

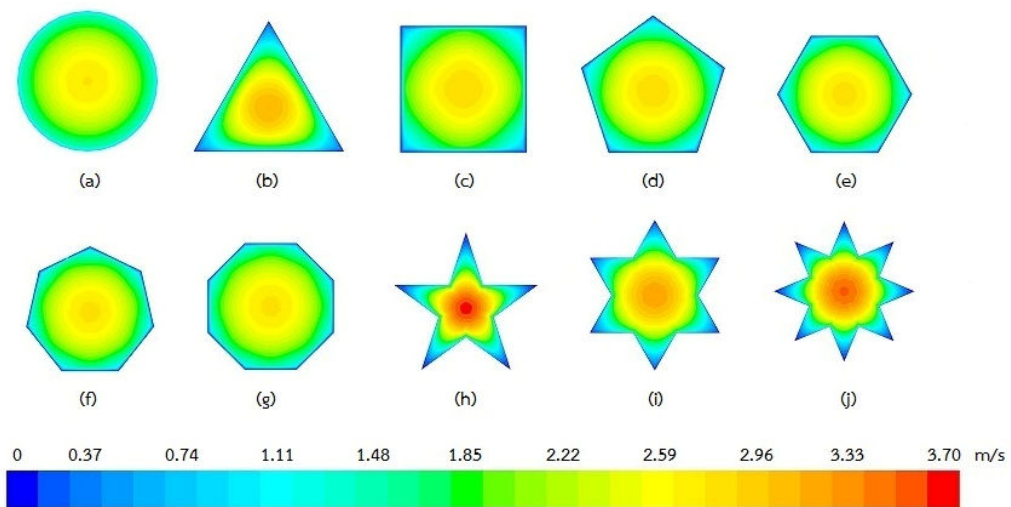


**Figure C.6** Axial velocity contours of microfiltration membrane (outlet) at TMP = 0.5 bar: (a) circle, (b) triangle, (c) square, (d) pentagon, (e) hexagon, (f) heptagon, (g) octagon, (h) pentagram, (i) hexagram, and (j) octagram

APPENDIX E  
LIST OF PUBLICATION

Kritsana Saiyood, Eakarach Bumrunghthaichaichan, Santi Wattananuson,  
Walairat Chandra-ambhorn “CFD Modeling of Microfiltration Membrane with Seven  
Star-Shape Channels” Ladkrabang Engineering Journal, vol. 30, 2013.

# CFD Modeling of Microfiltration Membrane with Seven Star-shape Channels

Kritsana Saiyood Eakarach Bumrunghthaichaichan  
Santi Wattananusorn Walairat Chandra-ambhorn  
Department of Chemical Engineering, Faculty of Engineering,  
King Mongkut's Institute of Technology Ladkrabang

## Abstract

FLUENT® CFD software was employed to simulate permeate flux in microfiltration membrane with seven star-shape channels. The effects of turbulence model and face interpolation scheme were studied to achieve the optimal model. Three different types of k-epsilon model, including standard k-epsilon (SKE), renormalization group k-epsilon (RNGKE), and realizable k-epsilon (RKE), were used to model the turbulence. The simulated results revealed that the RNGKE turbulence model with second order upwind scheme was the optimal modeling of this simulation because of solution accuracy and time efficiency.

**Keywords:** CFD, microfiltration membrane, k-epsilon model

## 1. Introduction

Computational Fluid Dynamics (CFD) is an important scientific tool consisting of numerical method and algorithm to solve and analyze various fluid flow problems. Typically, fluid flow phenomena are governed by three fundamental physical laws, including the conservation of mass, the second Newton's law of motion, and the first law of thermodynamics. CFD is a useful tool because it can provide clear insight into various fluid flow phenomena with inexpensive operating cost.

Microfiltration is a process for separating particles with diameters between 0.1 and 10  $\mu\text{m}$  from

suspensions by moving liquid through a porous membrane. The performance of membrane filtration can be indicated by critical flux. There are many experimental and simulation works of membrane filtration. Chiu et al. [1-4] determined the critical flux enhancement method of ceramic membrane with seven star-shaped inlet channels, e.g. gas assisted, electrokinetic, baffles etc.

Pak et al. [5] used CFD technique with finite difference method to predict the growth rate of the concentration polarization boundary layer along the length of tubular membrane. The numerical results revealed that the local concentration boundary layer thickness found to

decrease with increasing axial Reynolds number or Schmidt number.

Wanthamane et al. [6] employed FLUENT® CFD code to investigate the effect of turbulence promoter geometry on flow pattern in ultra-filtration process. The results revealed that the maximum permeate flux was obtained by using the prism turbulence promoter.

The objective of this research was to determine the optimal turbulence model for modeling of microfiltration membrane with seven star-shape channels. The model was three-dimensional. The three different types of k-epsilon model, including SKE, RNGKE, and RKE, were employed to simulate fluid motions.

## 2. Governing Equations

All models were considered to be three-dimensional steady flow with constant kinematic viscosity. The flow system was governed by the continuity equation, momentum equation, and k-epsilon turbulence model.

The time average equations for the continuity equation and momentum equation can be written in the following form.

Continuity equation:

$$\frac{\partial \rho}{\partial t} + \nabla \cdot \bar{\mathbf{U}} = 0 \quad (1)$$

Momentum equation:

$$\frac{\partial (\rho \bar{\mathbf{U}})}{\partial t} + \nabla \cdot (\rho \bar{\mathbf{U}} \bar{\mathbf{U}}) = -\nabla \bar{p} + \nabla \cdot \bar{\boldsymbol{\tau}} + S_M \quad (2)$$

where  $\bar{\mathbf{U}} = \bar{u} \mathbf{i} + \bar{v} \mathbf{j} + \bar{w} \mathbf{k}$

The k-epsilon model includes two extra transport equations to represent the turbulent properties of the flow. The first equation is transport equation of turbulent kinetic energy ( $k$ ) and the second one is transport equation of dissipation rate of turbulent kinetic energy ( $\epsilon$ ). These two equations of SKE can be written as follows.

$k$ -transport equation:

$$\frac{\partial}{\partial t} (\rho k) + \frac{\partial}{\partial x_i} (\rho k u_i) = \frac{\partial}{\partial x_j} \left[ \left( \mu + \frac{\mu_t}{\sigma_k} \right) \frac{\partial k}{\partial x_j} \right] + G_k + G_b - \rho \epsilon - Y_M + S_k \quad (3)$$

$\epsilon$ -transport equation:

$$\frac{\partial}{\partial t} (\rho \epsilon) + \frac{\partial}{\partial x_i} (\rho \epsilon u_i) = \frac{\partial}{\partial x_j} \left[ \left( \mu + \frac{\mu_t}{\sigma_\epsilon} \right) \frac{\partial \epsilon}{\partial x_j} \right] + C_{1\epsilon} \frac{\epsilon}{k} (G_k + C_{3\epsilon} G_b) - C_{2\epsilon} \rho \frac{\epsilon^2}{k} + S_\epsilon \quad (4)$$

where  $\mu_t = \rho C_\mu \frac{k^2}{\epsilon}$ ,  $G_k = -\rho \overline{u'_i u'_j} \frac{\partial \bar{u}_j}{\partial x_i}$ ,

$G_b = \beta g_i \frac{\mu_t}{Pr_t} \frac{\partial T}{\partial x_i}$ ,  $Y_M = 2\rho \epsilon M_i^2$ ,  $C_{3\epsilon} = \tanh \left| \frac{v}{u} \right|$

The model constants in these equations are shown in Table 1.

**Table 1** Standard k-epsilon model constants

$C_{1\epsilon}$	$C_{2\epsilon}$	$C_\mu$	$\sigma_k$	$\sigma_\epsilon$
1.44	1.92	0.09	1.0	1.3

The two transport equations of RNGKE and RKE are slightly different from SKE. The details of these two turbulence models are published in ANSYS FLUENT Theory Guide [7].

In order to simulate fluid motion in porous media (membrane) the

momentum source term was applied. This membrane was assumed to be a homogeneous porous media. The momentum source term of this assumption, which consisted of two parts including the viscous loss term and inertial loss term, was given by

$$S_i = - \left( \frac{\mu}{\alpha} v_i + C \frac{1}{2} \rho |v| v_i \right) \quad (9)$$

where  $S_i$  is the momentum source term in  $i$ -direction.

### 3. Numerical method

The modeling was based on the experiment conducted by Chiu et al. [2]. These three-dimensional models were performed by GAMBIT. The system is a tubular membrane with seven star-shape inlet channels. The tubular membrane diameter and length are 20 mm and 300 mm, respectively. The hydraulic diameter, which is commonly used in non-circular tubes, of these star channels are 2.3 mm. The water inlet was assumed to be uniform with velocity of 2 m/s. The kinematic viscosity of water is  $1 \times 10^{-6} \text{ m}^2/\text{s}$ . At the wall, no-slip boundary condition was applied. The fluid motion in star-shape channels and membrane were considered to be turbulent and laminar flow, respectively. In other words, the fluid motion in membrane was only dominated by viscous resistance. The boundary conditions are depicted in Fig. 1.

Grid independent solution study was achieved by using the model with 3,878,400 hexahedral cells. The grid

generation of the model is shown in Fig 2.

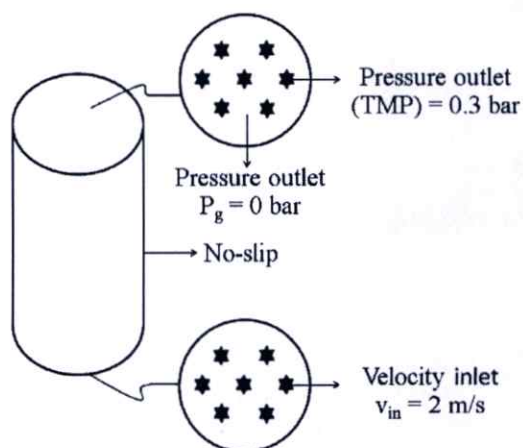


Fig. 1 Boundary conditions

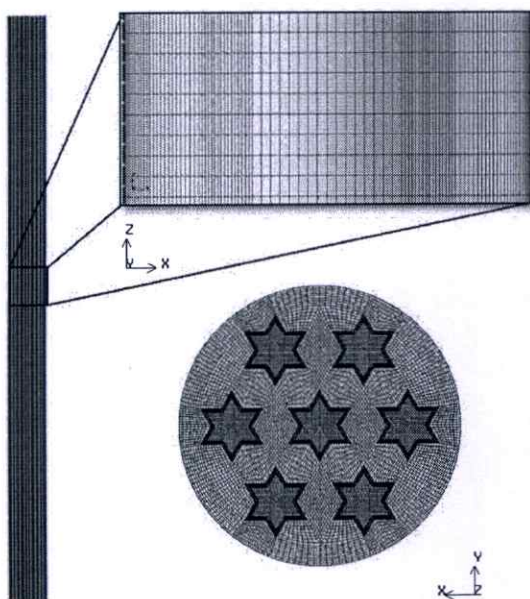


Fig. 2 Grid generation

Governing equations were solved numerically by using FLUENT® CFD code, which based on Finite Volume Method (FVM). For this study, the pressure-velocity coupling was SIMPLE algorithm. The interpolation scheme for pressure and turbulent quantities were standard and first order upwind, respectively.

These models were performed by using personal computer with Intel(R) Core(TM) i7-4770 (3.4 GHz) and 16 GB installed memory.

## 4. Results and Discussion

### 4.1 Model validation

In order to verify CFD simulation, the cross-flow microfiltration with inlet velocity of 2 m/s and trans-membrane pressure (TMP) of 0.3 bar was simulated. SKE was adopted to simulate turbulence. The size of membrane and geometric were identical as those depicted in Ref. [2]. The simulated permeate flux and experimental data were in acceptable level with the error of 10.79%.

### 4.2 Effect of k-epsilon model

The effect of three different types of k-epsilon model, including SKE, RNGKE, and RKE, was studied. The predicted volumetric flux and velocity contours at the channel outlet of these models are shown in Table 2 and Fig. 3, respectively. The results revealed that RKE was the best model to predict the volumetric flux with the error of 0.36%. The velocity magnitude contour of RKE was smoother than others as depicted in Fig. 3. However, the calculation time of RKE was higher than others (38 times for SKE and 23 times for RNGKE).

The velocity profiles of these models were slightly different. The SKE showed top-hat velocity profile as shown in Fig. 4. Typically, the channel flow shows the maximum velocity at the channel center and velocity decreases with increasing the

distance from the channel center. The deviation of the SKE result was due to the absence of secondary flow calculation [7]. In other words, the RNGKE and RKE were more accurate to calculate the secondary flow than SKE.

In engineering applications, the accuracy and calculation time need to be compromised. As mentioned earlier, the calculation time of SKE and RNGKE were extremely less than RKE. In addition, the RNGKE was more accurate than SKE. Thus, RNGKE was the suitable model for this situation.

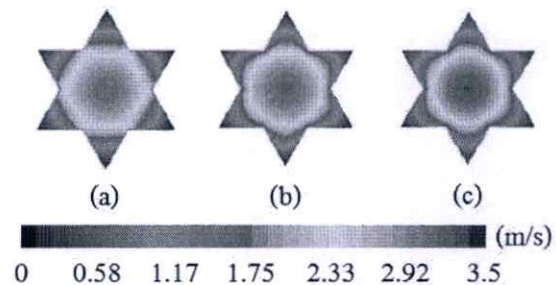


**Fig. 3** Velocity magnitude contours (TMP=0.3 bar) at outlet center star channel of (a) SKE (b) RNGKE and (c) RKE

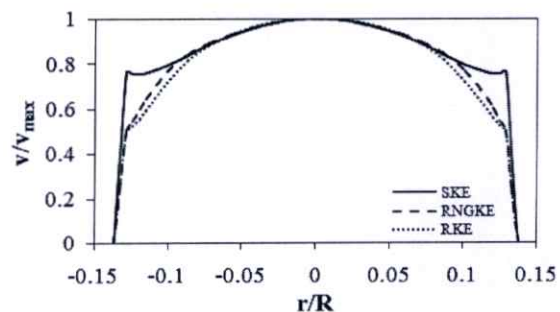


**Fig. 4** The comparison between the dimensionless velocity magnitude ( $v/v_{max}$ ) at channel center ( $z = 0.15$  m) of 3 k-epsilon models for different dimensionless radial distance ( $r/R$ )

**Table 2** The predicted volumetric flux for different turbulence models

Model	Volumetric flux ( $\text{m}^3/(\text{m}^2\cdot\text{s})$ )	Error (%)	Calculation time (hour)
Exp	$2.79 \times 10^{-5}$	-	-
SKE	$2.52 \times 10^{-5}$	10.71	6
RNGKE	$2.9 \times 10^{-5}$	3.94	10
RKE	$2.8 \times 10^{-5}$	0.36	230

**Table 3** The predicted volumetric flux for different schemes

Model	Volumetric flux ( $\text{m}^3/(\text{m}^2\cdot\text{s})$ )	Error (%)	Calculation time (hour)
FOU	$2.44 \times 10^{-5}$	14.34	6
SOU	$2.52 \times 10^{-5}$	10.71	6
QUICK	$2.52 \times 10^{-5}$	10.71	6
TOM	$2.52 \times 10^{-5}$	10.71	6

#### 4.3 Effect of momentum scheme

According to finite volume method (FVM), the interpolation of face values is required. In this simulation, the momentum numerical scheme, including first order upwind (FOU), second order upwind (SOU), QUICK, and third order MUSCL (TOM), were simulated to obtain the suitable scheme for this simulation.

The fluid motion of this simulation is turbulent flow ( $Re = 4,600$ ). In turbulent flow, the inertia force is dominated. In other words, the turbulent flow depends on convective term. The simulated results revealed that the SOU and higher order schemes (error = 10.71%) were more accurate than FOU (error = 14.34%) as shown in Table 3. In other words, the higher order schemes were required to indicate the strongly convective flow from upstream.

Among higher order schemes, the SOU was the optimal scheme because it could predict the volumetric flux with the error of 10.71% and required less calculation time.

## 5. Conclusions

The modeling of microfiltration membrane with seven star-shape channels can be simulated by using FLUENT®. Three types of k-epsilon model have been applied to simulate turbulence. The preliminary simulated flux was in good agreement with the experimental data [2].

The simulation results revealed that the RNGKE with SOU was the suitable model of this situation because RNGKE produced the accurate solution with reasonable time consumption.

## 6. Nomenclatures

### 6.1 Alphabetical Symbols

- $G_b$  The generation of turbulence due to buoyancy
- $G_k$  The production of turbulence kinetic energy
- $g$  Gravitational constant
- $k$  Turbulent kinetic energy
- $M_t$  Turbulent Mach number
- $\bar{p}$  Mean pressure
- $S_k$  Turbulent kinetic energy source term

$S_\epsilon$	Dissipation rate of turbulent kinetic energy source term
$\bar{u}$	Mean x-velocity
$\bar{v}$	Mean y-velocity
$\bar{w}$	Mean z-velocity
$\gamma_M$	Dilatation dissipation term

## 6.2 Greek Symbols

$\beta$	Thermal expansion coefficient
$\epsilon$	Dissipation rate of turbulent kinetic energy
$\mu$	Viscosity
$\mu_t$	Turbulent viscosity
$\mu_{eff}$	Effective viscosity
$\rho$	Fluid density

## 7. References

- [1] T. Y. Chiu, A. E. James, "Critical flux determination of non-circular multi-channel ceramic membranes using  $TiO_2$  suspensions," *Journal of Membrane Science*, vol. 254, pp. 295–301, 2005.
- [2] T. Y. Chiu, A. E. James "Critical flux enhancement in gas assisted microfiltration," *Journal of Membrane Science*, vol. 281, pp. 274–280, 2006.
- [3] T. Y. Chiu, A. E. James, "Effects of axial baffles in non-circular multi-channel ceramic membranes using organic feed," *Separation and Purification Technology*, vol. 51, pp. 233–239, 2006.
- [4] T. Y. Chiu, A. E. James, "Electrokinetic characterisation of cleaned non-circular multi-channelled membranes," *Desalination*, vol. 189, pp. 13–20, 2006.
- [5] A. Pak, T. Mohammadi, S. M. Hosseinalipour, V. Allahdini, "CFD modeling of porous membranes," *Desalination*, Vol. 222, pp.482–488, 2008.
- [6] S. Wanthamane, E. Bumrungrthaichaichan, S. Wattananusorn, "Influence of Turbulence Promoter Geometry on Flow Pattern in Cross-Flow Membrane Ultrafiltration," *Ladkrabang Engineering Journal*, Vol. 29, pp. 48-53, 2012.
- [7] Ansys, Inc. "Theory Guide," pp. 49-62, 2011.

## VITA

NAME	Mr. Kritsansa Saiyood
DATE OF BIRTH	December 25, 1987
EDUCATIONAL RECORD	
HIGH SCHOOL	High School Graduation Takphittayakhom School, 2005
BACHELOR'S DEGREE	Bachelor of Engineering (Chemical Engineering) Mahidol University, 2009
MASTER'S DEGREE	Master of Engineering (Chemical Engineering) King Mongkut's Institute of Technology Ladkrabang, 2014